Cell Reports

Article

Mitochondria-rough-ER contacts in the liver regulate systemic lipid homeostasis

Graphical abstract

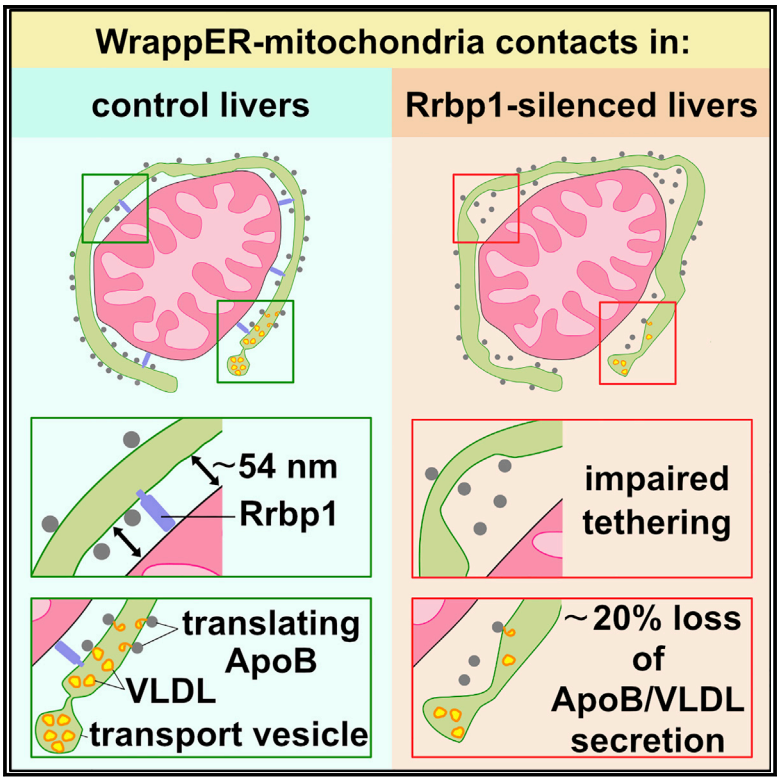

Highlights

- Liver mitochondria are extensively wrapped by curved sheets of rough ER (wrappER)
- The wrappER is enriched in fatty acid and VLDL transcripts, proteins, and particles
- WrappER-mitochondria contacts regulate VLDL synthesis and respond to lipid flux changes
- WrappER-mitochondria contacts contain MAMs and sites of adhesion between organelles

Authors

Irene Anastasia, Nicolò Ilacqua, Andrea Raimondi, ..., Eugene V. Koonin, Luca Scorrano, Luca Pellegrini

Correspondence

luca.pellegrini@fmed.ulaval.ca

In brief

Anastasia et al. characterize the contact established by a curved wrapping-type of rough ER (wrappER) with mitochondria and discover that this inter-organellar association is dynamic, regulated by lipid fluxes, and necessary for correct hepatic synthesis and secretion of very-low-density lipoproteins.

Anastasia et al., 2021, Cell Reports *34*, 108873
March 16, 2021
https://doi.org/10.1016/j.celrep.2021.108873

CellPress

Cell Reports

CellPress
OPEN ACCESS

Article

Mitochondria-rough-ER contacts in the liver regulate systemic lipid homeostasis

Irene Anastasia,[1,2,14] Nicolò Ilacqua,[1,2,14] Andrea Raimondi,[3] Philippe Lemieux,[2] Rana Ghandehari-Alavijeh,[2] Guilhem Faure,[4,5] Sergei L. Mekhedov,[5] Kevin J. Williams,[6] Federico Caicci,[7] Giorgio Valle,[7] Marta Giacomello,[7] Ariel D. Quiroga,[8,9] Richard Lehner,[9] Michael J. Miksis,[10] Katalin Toth,[11] Thomas Q. de Aguiar Vallim,[6,12] Eugene V. Koonin,[5] Luca Scorrano,[7] and Luca Pellegrini[2,13,15,*]

[1]Graduate Program in Neuroscience, Faculty of Medicine, Laval University, Quebec, QC, Canada
[2]Mitochondria Biology Laboratory, Brain Research Center, Quebec, QC, Canada
[3]Experimental Imaging Center, San Raffaele Scientific Institute, Milan, Italy
[4]Broad Institute of MIT and Harvard, Cambridge, MA, USA
[5]National Center for Biotechnology Information, NLM, NIH, Bethesda, MD, USA
[6]Department of Biological Chemistry, Geffen School of Medicine, UCLA, Los Angeles, CA, USA
[7]Department of Biology, University of Padua, Padua, Italy
[8]Instituto de Fisiología Experimental, CONICET, UNR, Rosario, Argentina
[9]Department of Pediatrics, University of Alberta, Edmonton, AB, Canada
[10]Department of Engineering Science and Applied Mathematics, Northwestern University, Evanston, IL, USA
[11]Department of Cellular and Molecular Medicine, University of Ottawa, Ottawa, ON, Canada
[12]Department of Medicine, Division of Cardiology, UCLA, Los Angeles, CA, USA
[13]Department of Molecular Biology, Medical Biochemistry and Pathology, Faculty of Medicine, Laval University, Quebec, QC, Canada
[14]These authors contributed equally
[15]Lead contact
*Correspondence: luca.pellegrini@fmed.ulaval.ca
https://doi.org/10.1016/j.celrep.2021.108873

SUMMARY

Contacts between organelles create microdomains that play major roles in regulating key intracellular activities and signaling pathways, but whether they also regulate systemic functions remains unknown. Here, we report the ultrastructural organization and dynamics of the inter-organellar contact established by sheets of curved rough endoplasmic reticulum closely wrapped around the mitochondria (wrappER). To elucidate the *in vivo* function of this contact, mouse liver fractions enriched in wrappER-associated mitochondria are analyzed by transcriptomics, proteomics, and lipidomics. The biochemical signature of the wrappER points to a role in the biogenesis of very-low-density lipoproteins (VLDL). Altering wrappER-mitochondria contacts curtails VLDL secretion and increases hepatic fatty acids, lipid droplets, and neutral lipid content. Conversely, acute liver-specific ablation of *Mttp*, the most upstream regulator of VLDL biogenesis, recapitulates this hepatic dyslipidemia phenotype and promotes remodeling of the wrappER-mitochondria contact. The discovery that liver wrappER-mitochondria contacts participate in VLDL biology suggests an involvement of inter-organelle contacts in systemic lipid homeostasis.

INTRODUCTION

Cellular functional systems are involved in either intracellular or systemic (organism-level) functions. Inter-organelle contacts typically regulate intracellular processes (de Brito and Scorrano, 2008; Chang et al., 2019; Dong et al., 2016; Lee et al., 2020; Vance, 2020; Wong et al., 2018). For example, the juxtaposition of mitochondria and smooth endoplasmic reticulum (sER), or MAM (mitochondria-associated ER membranes), the first functionally characterized inter-organellar contact (Vance, 1990), governs phospholipid biosynthesis and transport and Ca^{2+} transfer between these organelles (Rizzuto et al., 1998; Vance, 1990). However, a major component of animal evolution was the emergence of cellular activities that coordinate systemic functions (Arendt, 2008; Galluzzi et al., 2018). For example, in the pancreas, α and β cells secrete glucagon, insulin, and amylin to regulate blood glucose homeostasis; similarly, in the liver, hepatocytes secrete lipoproteins to regulate lipid homeostasis. However, whether inter-organelle contacts participate in the regulation of systemic functions remains unknown.

Liver cells have to regulate two types of lipid fluxes (Fu et al., 2012). The first type is intracellular, distributing lipids among organelles to maintain cellular homeostasis. The second type of flux is systemic; in this case, through lipoprotein synthesis, secretion, and recycling, the hepatocyte distributes triglycerides (TAGs) and cholesterol to peripheral tissues to sustain animal physiology (Goldstein and Brown, 2015). Recent studies have highlighted the increasing importance of inter-organelle contacts

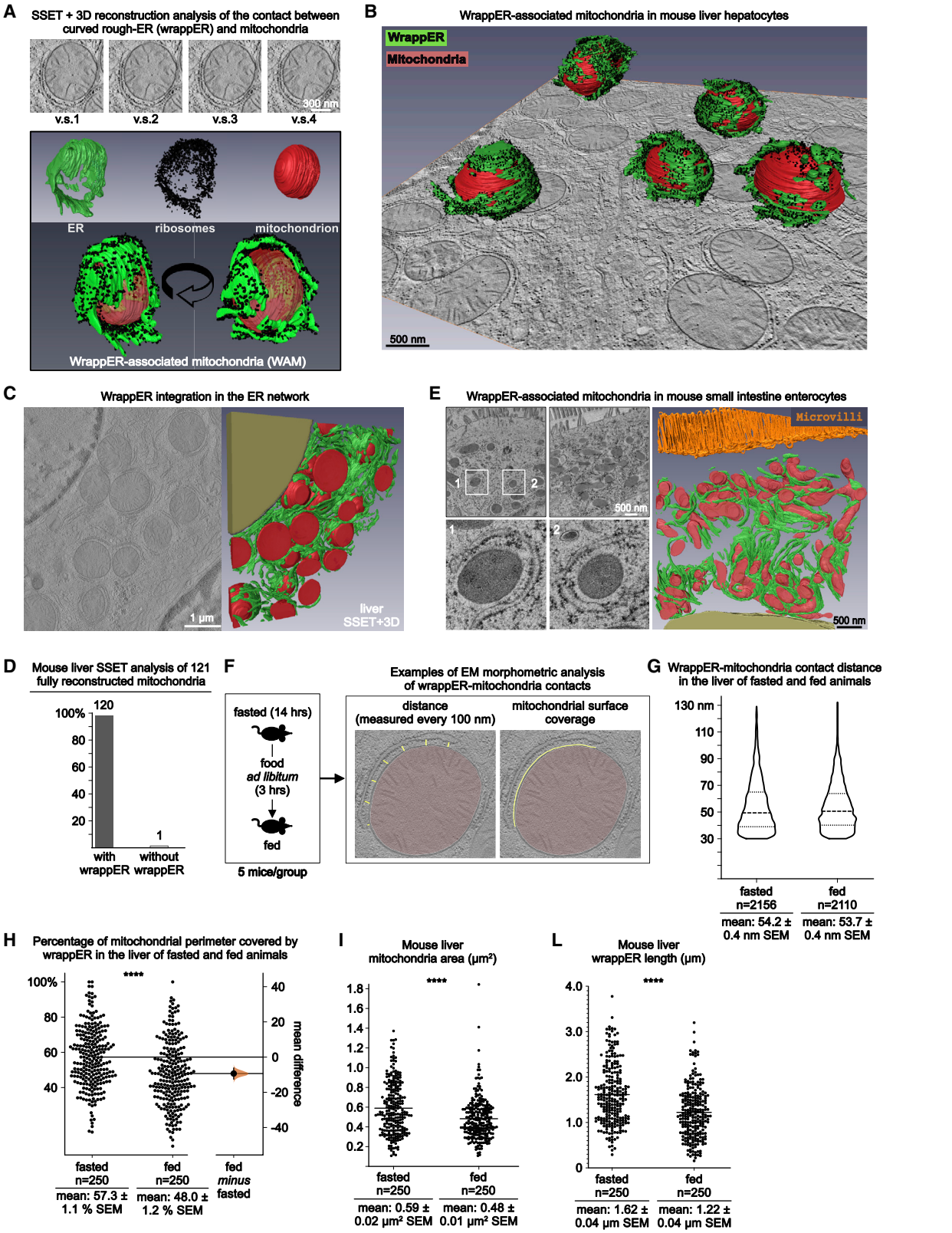

(legend on next page)

for intracellular lipid fluxes. For instance, cholesterol egress from lysosome to peroxisome, as well as from the endoplasmic reticulum (ER) to the plasma membrane and endocytic organelles, occurs through organized contacts between these organelles (Chu et al., 2015; Höglinger et al., 2019; Sandhu et al., 2018). However, whether and how inter-organelle contacts integrate intracellular lipid fluxes with systemic fluxes remains unknown.

Electron microscopy (EM) studies carried out in the 1950s highlighted the existence of contacts between different cellular organelles. The first to be described was the one between mitochondria and ergastoplasm, now commonly referred to as rough ER (rER) (Bernhard and Rouiller, 1956; Franke and Kartenbeck, 1971; Montisano et al., 1982). More recently, this inter-organellar contact has been observed in cultured cells (Wang et al., 2015), found to be chronically enriched in hepatocytes (Arruda et al., 2014), and shown to be tethered by the Synj2bp/Rrbp1 protein complex (Hung et al., 2017). However, its ultrastructural characterization, dynamics, and function(s) remain unknown, primarily because there are currently no established methods to isolate intact mitochondria associated with rER.

In this work, we studied mitochondria-rER contacts *in vivo* by serial section electron tomography (SSET) and 3D reconstruction analysis of cryo-fixed mouse tissue samples. We characterized this inter-organelle association as mitochondria tightly wrapped by sheets of curved rER (wrappER). Further, we used multi-omics and genetic approaches to obtain evidence that the wrappER is a distinct intracellular compartment and demonstrate the importance of wrappER-mitochondria contacts for very-low-density lipoprotein (VLDL) secretion from the liver, thereby connecting intracellular and systemic control mechanisms for lipid metabolism and homeostasis.

RESULTS

Mitochondria of liver hepatocytes and of small intestine enterocytes are wrapped by curved sheets of rER (wrappER)

Mouse liver SSET+3D analysis showed that nearly every mitochondrion of the hepatocyte was extensively wrapped by rER (n = 121). EM analysis validated and extended this finding to show that contacts between mitochondria and rER were nearly ubiquitous in livers of mice fasted overnight and fed for 3 h (Figures 1A–1D and S1A; Videos S1 and S2), indicating that the association between these two organelles is an integral structural parameter of the hepatocyte cellular organization.

Visual inspection of a large portion of the cell volume of hepatocytes reconstructed by SSET+3D analysis showed that the rER wrapping the mitochondria is not an isolated entity; rather, it is a type of curved rER that is seamlessly integrated into the ER network of the cell (Figure 1C; Video S2). Focused ion beam scanning electron microscopy analysis of 50 mitochondria from the mouse brain *corpus striatum* did not reveal associations between mitochondria and rER (data not shown); however, rER-mitochondria contacts were extensively present in mouse enterocytes (Figure 1E; Video S3), fatty-acid-absorbing epithelial cells of the small intestine that, similar to liver hepatocytes, but unlike brain cells, secrete Apolipoprotein B (ApoB) -containing lipoproteins (Dash et al., 2015; Hussain, 2000). Given the presence of this type of curved rER in cells of different developmental origins, as well as its characteristic property to tightly wrap substantial portions of mitochondria of various shapes and sizes, we denote it wrappER.

Fasting-to-feeding transitions regulate wrappER-mitochondria contacts in mouse liver

Given the presence of wrappER-mitochondria contacts in cell types that share a role in regulating dietary lipid uptake and systemic release, we investigated the dynamics of this inter-organelle association during fasting, when liver fatty acid absorption and VLDL synthesis and secretion are maximal, and at the time of refeeding (3 h postprandial), when these hepatic activities are substantially reduced (Wei et al., 2010). To this end, we used 2D-EM morphometric analysis to measure the two key structural parameters of the wrappER-mitochondria contact, namely, the percentage of the mitochondrial perimeter covered by the wrappER and the distance between the two organelles.

During fasting-refeeding, the mean wrappER-mitochondria distance remained approximately constant at 54 ± 0.4 nm (standard error of the mean [SEM]; n = ~2,100 from five mice; Figures 1F and 1G). However, the percentage of the mitochondrial perimeter covered by the wrappER decreased 16% upon refeeding (from 57.3% ± 1.1% to 48% ± 1.2%, SEM; $p < 0.0001$;

Figure 1. The mitochondria of liver hepatocytes and of small intestine enterocytes are wrapped by curved sheets of rough ER (wrappER)

(A) SSET+3D reconstruction of a mouse liver wrappER-mitochondria association. The top panel shows four consecutive virtual slices (v.s.) of a tomogram used for this analysis.

(B and C) SSET+3D reconstruction analysis showing extensive wrappER-mitochondria association and the integration of the wrappER into the ER network of the hepatocyte.

(D) SSET analysis showing that nearly all mouse liver mitochondria are in contact with the wrappER. Data obtained by visually inspecting 121 mitochondria originated from 10 tomograms obtained from four mouse livers.

(E) SSET+3D reconstruction analysis showing diffuse and extensive wrappER-mitochondria contacts in the enterocyte of the mouse small intestine.

(F) Examples of the method used to measure wrappER-mitochondria contact distance (every 100 nm; left EM image) and the percentage of mitochondrial perimeter covered by wrappER (right).

(G) WrappER-mitochondria distance in fasted and fed livers (median and quartiles are indicated; 50 wrappER-mitochondria contacts/liver; five livers/group). Note that MAM-like domains (10–30 nm) were not included in this analysis.

(H) Percentage of mitochondrial surface covered by wrappER ($p < 0.0001$; 50 wrappER-mitochondria contacts/liver; five livers/group). Right: estimation statistics analysis of the data; the mean difference between the groups is depicted as the dot within the vertical error bar that represents the 95% confidence interval.

(I and J) 2D-EM morphometric analysis. Area of the mitochondrial population (I) and average length of the wrappER (J) in fasted and fed livers ($p < 0.0001$; 50 mitochondria/mouse; five mice/group).

p values were calculated by Student's t test. Data were collected from mouse livers at 3 h postprandial unless otherwise indicated.

n = 250 from 5 mice; Figures 1F and 1H). Notably, the mitochondrial area also decreased 16% ($p < 0.0001$; Figure 1I), indicating that the loss of mitochondria perimeter covered by the wrappER results from a process that eliminates the contact between the organelles by reducing the size of the wrappER, which indeed is 25% shorter at 3 h postprandial ($p < 0.0001$; Figure 1L). Overall, these data indicate that although the association between wrappER and mitochondria is always present and extensive, the extent of the contact between these organelles is dynamically regulated by the metabolic changes that accompany the nutritional status of the animal, as also supported by its chronic enrichment in the livers of obese mice (Arruda et al., 2014).

The wrappER contains MAM-like domains and adhesion sites to the mitochondrial membrane

MAMs are domains of smooth ER that are closely juxtaposed with the mitochondrial outer membrane (10–30 nm) and coordinate the fluxes of phospholipids and calcium between the organelles (Giacomello and Pellegrini, 2016; Rizzuto et al., 1998; Vance, 1990). MAMs are present and dynamically regulated in hepatocytes (Sood et al., 2014), where their function in phosphatidylserine (PS) transfer is necessary to avoid ER stress and nonalcoholic steatohepatitis (NASH)-like steatosis (Hernández-Alvarez et al., 2019). The widespread and extensive occurrence of contacts between mitochondria and wrappER prompted us to investigate the possibility that MAMs are domains of this interorganelle contact. To this end, we visually inspected 33 wrappER-associated mitochondria (WAMs) that were reconstructed, completely or partially, by SSET+3D analysis. We found that 91% of the WAMs contained at least one MAM-like domain (Figures 2A and 2B and S1B–S1D; Video S4) that, overall, occupied ~5% of the area of the wrappER and covered ~1.8% of the mitochondrial surface, a value similar to that measured in cultured cells (Csordás et al., 2006; Rizzuto et al., 1998). Noteworthy, 2D-EM morphometric analyses showed that over 60% of WAMs included at least one MAM-like domain (Figure 2C) but did not reveal mitochondria forming contacts with the smooth ER alone. We conclude that in the mouse liver, MAMs are an integral subdomain of the wrappER.

Further EM and SSET analysis of the wrappER-mitochondria contact identified the existence of areas where the membranes of the two organelles are attached, but not fused to each other. These areas, which we refer to as adhesion sites, have not been reported before but appear similar to the recently described contacts between ribosome-associated vesicles and mitochondria (Carter et al., 2020). Visual inspection of these adhesion sites showed that they are typically formed by protrusions of the mitochondria toward the wrappER (Figure 2D; Video S5) and do not appear to be fused with membranes. Their average size is smaller than that of MAMs (62 ± 3 nm versus 193 ± 6 nm SEM; Figure 2F), and their frequency remains constant during fasting-to-feeding transitions (Figure 2E).

Altogether, these ultrastructural observations show that the wrappER-mitochondria contact consists of at least three distinct domains: MAM-like structures, the ribosomes-containing space between the organelles that accounts for most of the interorganelle contact volume, and adhesion sites where the membranes of the two organelles come into direct physical contact.

Contacts between rER-mitochondria and MAM-like phospholipid synthesis are preserved in mouse liver fractions enriched in WAMs

To investigate the function of the wrappER and the role of its association with mitochondria, we developed a protocol for the isolation of WAMs from the mouse liver. We took advantage of the considerable negative buoyancy of the WAMs when they are subjected to low *g* forces in a dense sucrose-containing medium. EM analysis of WAM-enriched fractions showed that they indeed contain mitochondria whose outer membrane is closely and evenly associated with curved rER (Figure 3B). Proteomic analysis of WAM-enriched fractions and of control ER-enriched fractions indicated that in the former, 78% of the detectable proteins were indeed from the two organelles we intended to copurify, namely, mitochondria (48%) and rER (30%) (n = 6; Figures 3A, 3C, S2A, and S2B; Table S1). These data, which we corroborated by immunoblot analysis (Figure 3A, right panel), are well within the range of previously published organelle-isolation protocols (Bayraktar et al., 2019; Benador et al., 2018; Gilchrist et al., 2006; Wyant et al., 2018).

WAM-enriched fractions also supported robust ^{3}H-serine incorporation and conversion into ^{3}H-PS and ^{3}H-phosphatidylethanolamine (PE), the signature biochemical reactions of the MAM (Vance, 1990) (Figures 3D and 3E). Thus, WAM-enriched fractions contain not only the long-ranging rER-mitochondria contacts but also well-characterized, short-ranging, functionally active MAMs, thereby recapitulating *in vivo* observations (Video S4). Taken together, these results indicate that WAM-enriched fractions are suitable for the functional characterization of mouse liver wrappER-mitochondria contacts.

Integrated omics analysis identifies a role of WAM-enriched fractions in systemic lipid homeostasis

The protocol developed to prepare WAM-enriched fractions was designed so as to retain actively translating ribosomes (phospho-S6; Figure 3A) and thus allowed not only proteomics but also simultaneous transcriptome analysis. Indeed, deep sequencing of the WAM-associated mRNAs followed by normalization for relative mitochondrial abundance (measured as reads of the mtDNA transcripts) identified 1,160 recurring mRNA species (n = 6; Figure S2C; Table S2).

To determine whether some of these mRNAs were enriched in WAM fractions, we also analyzed the transcriptome of the liver homogenates from which the WAM fractions were prepared. This analysis showed that WAM fractions contained 205 transcripts with levels of enrichment ranging from 20% to 34% of their expression level in the liver (0.5% ± 0.01% average SEM of enrichment per gene; Figures 3F and S2D; Table S2). Within this group, transcripts encoding ER proteins were the most abundant ones; in contrast, transcripts of nuclear-encoded mitochondrial proteins were conspicuously poorly represented (Figure S2E; Table S2).

The intersection between the transcriptomic and proteomic datasets defined a core subset of WAM proteins whose mRNAs were also enriched in the WAMs. A stringent filter identified 47 candidates, of which 35 were ER proteins (Figure 3G and S3A; Table S3). Interrogation of the Gene Ontology knowledgebase with the 47 candidate WAM genes also identified plasma

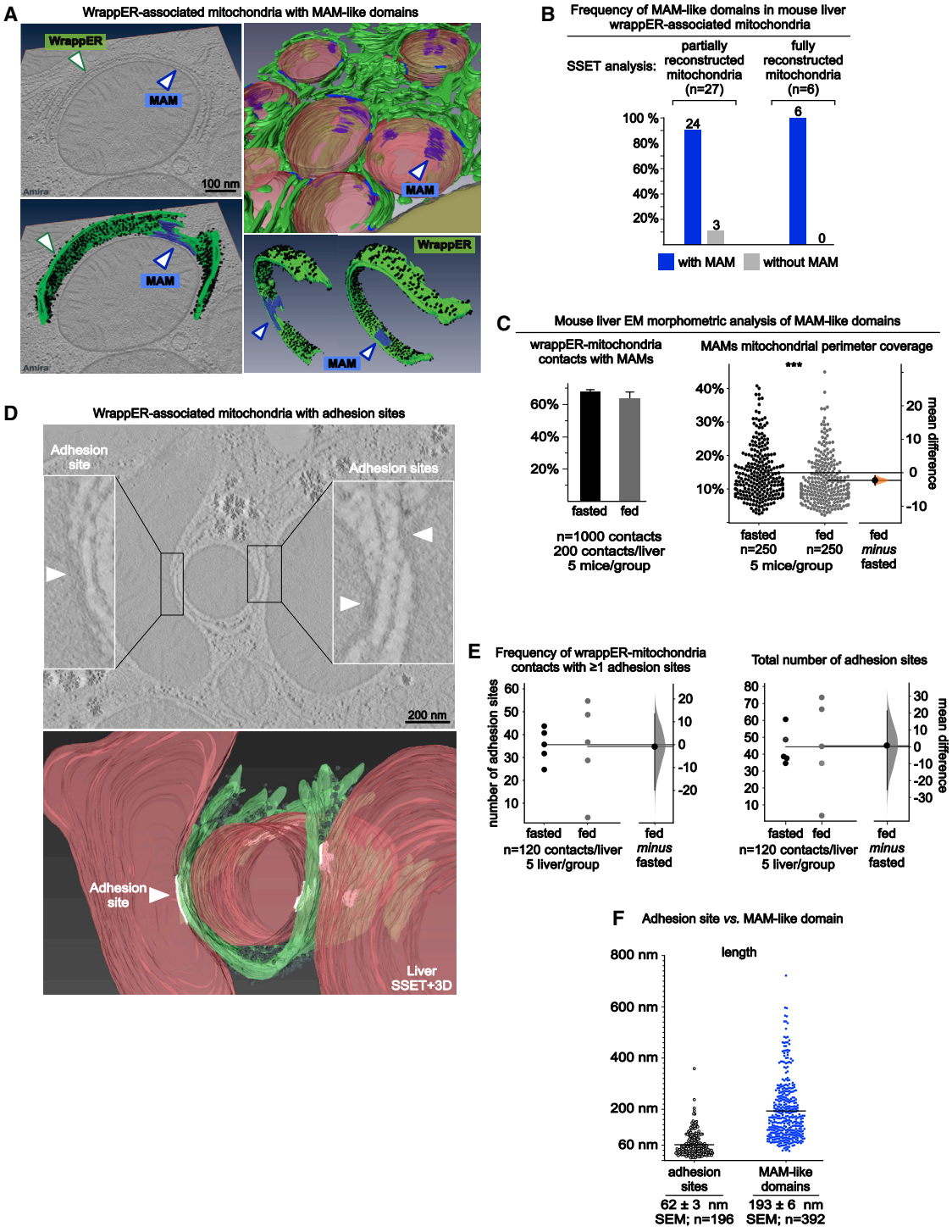

Figure 2. The wrappER contains MAM-like domains and sites of adhesion to the mitochondrial membrane

(A and B) SSET+3D reconstruction and quantitative analysis of the MAM-like domains (blue) embedded within wrappER-mitochondria contacts.

(C) 2D-EM quantitative morphometric analysis of the MAM-like domains embedded within wrappER-mitochondria contacts. Left: mean ± SEM; 200 contacts/mouse liver; five mice/group. Right: $p < 0.001$; 50 MAM-like domains/mouse liver; five mice/group. p values were calculated by Student's t test.

(D) Virtual slice of mouse liver WAMs showing sites of physical contact between wrappER and mitochondria (adhesion sites; white arrows).

(E and F) 2D-EM quantitative analysis of the adhesion sites embedded within wrappER-mitochondria contacts (n = 5 mice). Data were analyzed by estimation statistics (E); each point represents the number of observations recorded in each mouse liver analyzed (mean).

Data were collected from mouse livers at 3 h postprandial unless otherwise indicated.

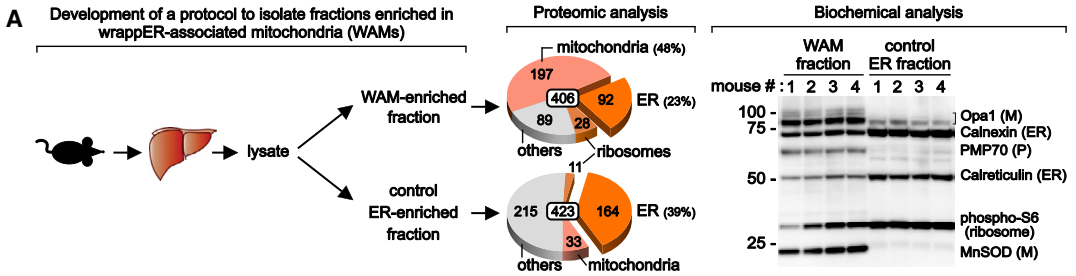

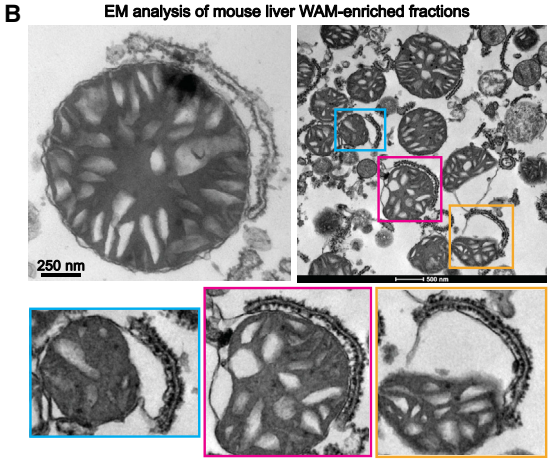

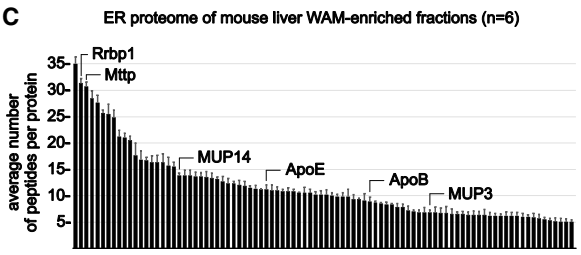

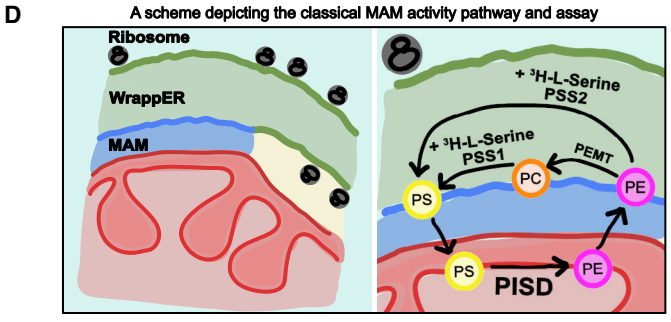

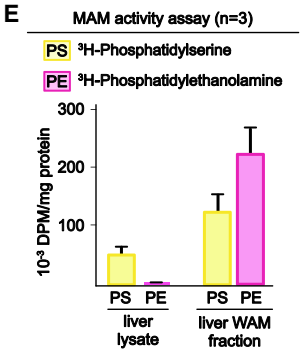

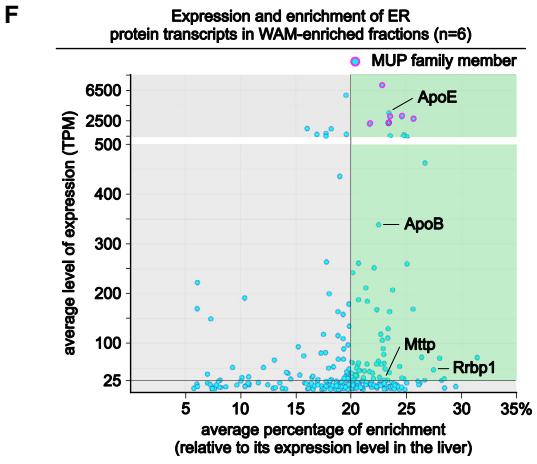

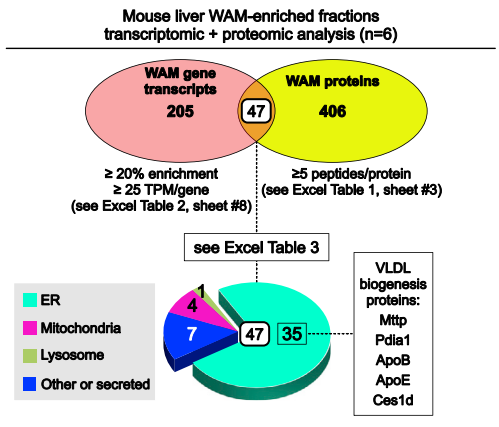

(legend on next page)

lipoprotein particle assembly as the most abundantly represented biological process in this compartment (Figure S3A). Consistent with this observation, Mttp, Pdia1, ApoB, and ApoE, the key determinants of VLDL biogenesis (Shelness and Sellers, 2001), as well as Ces1d, a luminal ER lipase involved in VLDL quality control (Wei et al., 2010), were among the most abundant WAM transcripts and proteins (Figures 3C, 3F, 3G, and S3B–S3D).

Members of the major urinary protein (MUP) family were also highly enriched in WAM fractions (Figures 3C, 3F, and 4A). The MUP family members are highly similar secreted proteins that belong to the lipocalin protein superfamily (Figure S4A). They contain a conserved N-terminal ER signal peptide and are closely related to PTGDS (Figure S4A), a fatty-acid-binding protein (Zhou et al., 2010). Superposition of the structure of MUP1 over the structure of PTGDS complexed with palmitic acid suggested that the hydrophobic cavity of MUP could accommodate a palmitate molecule (Figures 4B-4F). Comparative lipidomic analysis indeed indicated that WAMs contained a ∽30% excess of palmitate and other free fatty acids (FFAs) over the control mouse liver ER-enriched fractions ($p < 0.0001$; $n = 10$; Figure 4G; Table S4).

Altogether, the integrated omics analysis of WAM-enriched fractions supports a role of the wrappER-mitochondria compartment in systemic liver lipid homeostasis.

WrappER is a site of VLDL biogenesis in mouse liver

To validate the participation of the wrappER in systemic lipid homeostasis, we employed a combination of approaches to demonstrate that this type of ER is a bona fide site of VLDL biogenesis. First, we used immunogold EM analysis on WAM-enriched fractions to demonstrate the localization of Mttp, the most upstream regulator of VLDL biogenesis (Chang et al., 1999; Raabe et al., 1999; Wetterau et al., 1990; Raabe et al., 1998), at the wrappER (Figures 5A and S5A). On the wrappER membrane, we also immunolocalized ApoB, the core VLDL component (Figures 5B and S5B), a finding that is consistent with current data on ApoB translation and translocation and its role in the initiation of VLDL assembly (Shelness et al., 1999). These findings support the results obtained from the transcriptomic and proteomic analysis by demonstrating the presence of key components of the VLDL biogenesis pathway at the wrappER.

Second, we returned to our mouse liver SSET+3D analysis of the wrappER in order to inspect its membrane and lumen for the presence of lipid lens and of VLDL-like particles. This analysis indeed showed that the phospholipid bilayer of the wrappER membrane widened into lens-shaped structures that are typically associated with neutral lipids accumulation (Walther et al., 2017) and VLDL assembly (Shelness et al., 1999) (Figures 5C, 5D, and S5C; Video S6). Similarly, VLDL-like particles were observed within the wrappER lumen (Figure 5D; Video S6) as well as inside a vesicular structure that appeared to be budding from the wrappER and resembled VLDL-transport vesicles (Siddiqi, 2008) (Figure 5E; Video S6).

Third, we identified by immunogold negative staining VLDL particles isolated from WAM-enriched fractions. In this experiment, we gently broke WAM fraction membranes by freezing and thawing and floated lipoprotein particles using very high *g* forces. Next, we analyzed the isolated particles by negative staining coupled to anti-ApoB immunogold EM analysis (Syed et al., 2017). This experiment identified anti-ApoB-decorated particles with a diameter of 34.8 ± 0.6 nm (SEM) which is consistent with the size of nascent VLDL (Yu et al., 2016) (Figure 5F).

Lastly, we returned to the lipidomic analysis and confirmed the presence of the signature components of lipoproteins, TAGs, and cholesteryl esters (CEs) in WAM-enriched fractions (Figure 4G; Table S4). The demonstration of the involvement of wrappER in VLDL biogenesis supports its participation in systemic lipid metabolism and suggests the possibility that the wrappER-mitochondria could also be required for hepatic lipid homeostasis.

Rrbp1 silencing modifies wrappER-mitochondria contacts

To address the role of wrappER-mitochondria contacts in hepatic lipid homeostasis, we first sought to identify potential regulators of this inter-organelle association by analyzing the transcriptomic and proteomic data for the WAM-enriched fractions. The ER membrane protein Rrbp1 (ribosome-binding protein 1) that has been shown to function as the ribosome receptor (Langley et al., 1998; Wanker et al., 1995) emerged as a plausible candidate given its previously proposed role as a rER-mitochondria tether in cultured cells (Hung et al., 2017) as well as its substantial enrichment in mouse liver WAM-containing fractions (28% mRNA enrichment; 31 ± 1 peptides/protein; Figures 3C and 3F). Consistent with this possibility, comparative immunoblot analysis showed that mouse liver WAM-enriched fractions, but not control ER-enriched fractions, expressed unique isoforms of Rrbp1. More specifically, WAM-enriched fractions contained

Figure 3. A compendium of ER transcripts and proteins present in mouse liver WAM-enriched fractions

(A) Summary of the proteomic and biochemical analysis performed on WAM-enriched fractions and, as a control, on ER-enriched fractions. M, mitochondria; P, peroxisome.

(B) Micrographs of WAM-enriched fractions showing the preservation of wrappER-mitochondria contacts.

(C) Schematic representation of the 92 ER proteins identified by the proteomic analysis of WAM-enriched fractions. Each bar represents a protein (mean ± SEM; n = 6; Table S1). The proteins addressed in this study are shown.

(D and E) MAM-like phospholipid synthesis is preserved in mouse liver fractions enriched in wrappER-associated mitochondria (WAMs). (D) MAM pathway for phosphatidylethanolamine (PE) synthesis and assay. (E) Level of PE synthesis measured in mouse liver lysate and WAM fractions (mean ± standard deviation [SD]; n = 3).

(F) ER transcripts identified by the transcriptomic analysis of WAM-enriched fractions. The y axis indicates the gene average level of expression (as number of transcripts per million), and the x axis its level of enrichment relative to its expression level in mouse liver lysates (n = 6). The transcripts encoding for the proteins addressed in this study are shown. See also Table S2.

(G) Summary of the transcriptomic and proteomic analysis done on WAM-enriched fractions. The Venn diagram shows the 47 highly expressed proteins whose transcript were also highly enriched in the WAM-enriched fractions.

Data collected from mouse livers at 3 h postprandial.

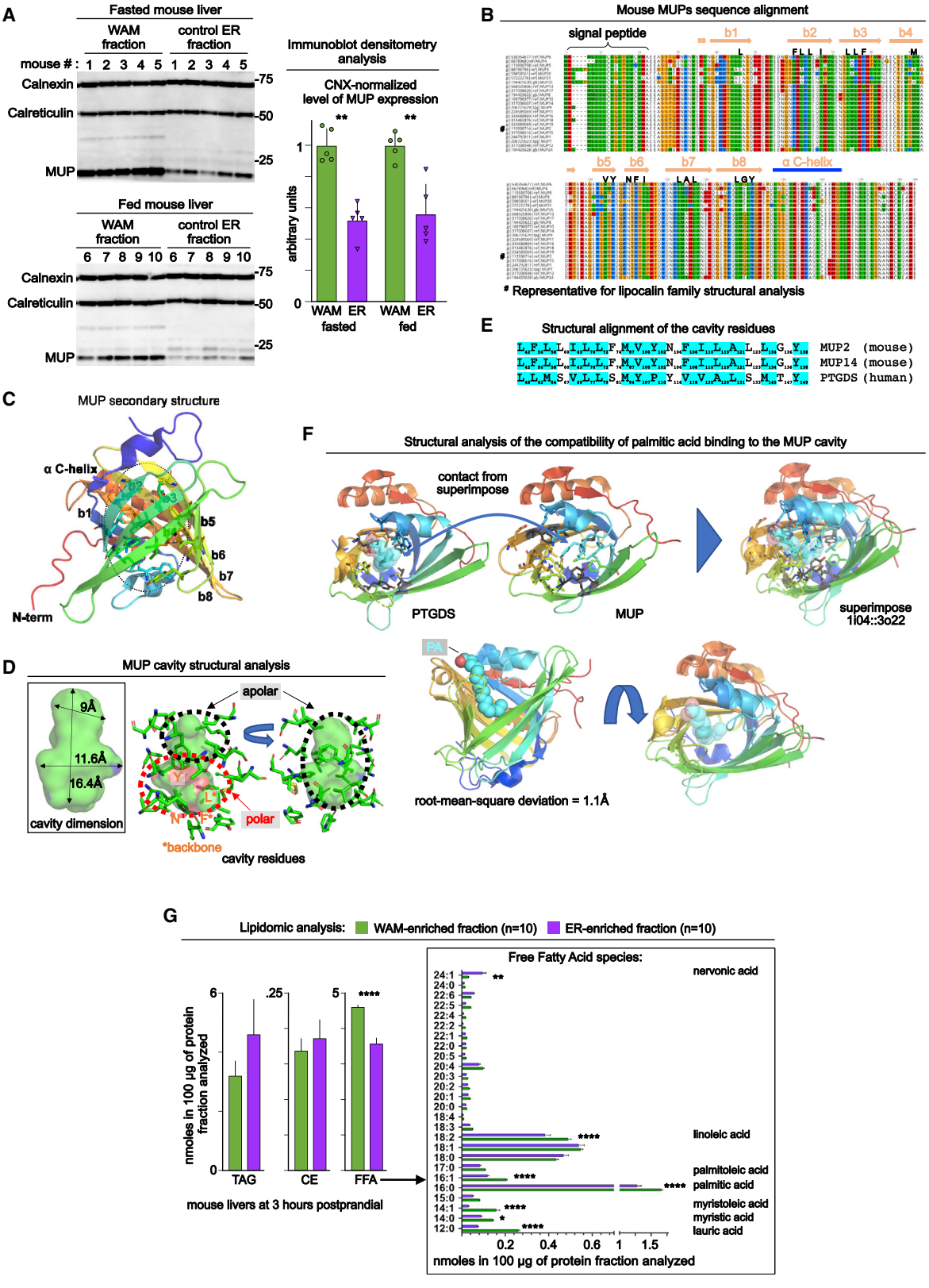

(legend on next page)

a 100-kDa isoform that is barely detectable in ER-enriched control fractions and that appears to be under metabolic control because its expression level is higher during fasting. Similarly, whereas WAM- and ER-enriched fractions both expressed a 90-kDa isoform of Rrbp1, this shorter isoform accumulated in large amounts during refeeding only in WAM-containing samples (Figures 6A and S6A). Among the identified alternative splice isoforms of mouse Rrbp1, there are six that are within the 90-kDa to 100-kDa size range and recognized by the anti-Rrbp1 antibody used in this work (Table S6; Data S1) (Kim et al., 2000). The Rrbp1 gene encodes a region that consists of 61 lysine-rich decapeptide repeats that are implicated in ribosome binding (Langley et al., 1998; Wanker et al., 1995). The longest Rrbp1 isoforms contain all these repeats; however, in the 90-kDa to 100-kDa forms, the portion of the transcript encoding the repeats is spliced out as an alternative intron (in one form, leaving seven repeats intact; Table S6; Data S1). Which Rrbp1 isoforms are specifically enriched in the WAMs remains to be determined, but the absence of the lysine-rich repeats that are implicated in ribosome binding (Langley et al., 1998; Wanker et al., 1995) is compatible with the functions of these forms being distinct from that of a ribosome receptor, such as the tethering function. Altogether, these data indicate that specific isoforms or post-translationally modified variants of Rrbp1 accumulate and are metabolically regulated in WAM-containing fractions.

Because biophysical modeling of the wrappER-mitochondria contact indicated that the association between these organelles must occur via tethers (see energy balance model of the wrappER-mitochondria contact in STAR Methods) and anti-Rrbp1 immunogold labeling localized Rrbp1 at the interface between the wrappER and mitochondria (Figures 6B, S6C, and S6D), we next addressed the potential role of Rrbp1 as a regulator of the wrappER-mitochondria contact organization *in vivo*. To this end, we silenced Rrbp1 expression in the liver by tail-vein injection of adeno-associated virus serotype 8 (AAV8) carrying a GFP marker and a small hairpin RNA (shRNA) against Rrbp1. Within 3 weeks of viral transduction, GFP expression in the liver was almost ubiquitous (Figure S6E), and the expression of the Rrbp1 protein, analyzed by immunoblot and quantitative proteomic studies, was reduced by at least 50% (Figures 6C, S6A, and S6B).

To assess the effect of Rrbp1 silencing on the organization of the wrappER-mitochondria contact, we analyzed five mouse livers in which Rrbp1 expression was reduced by ~70%. Visual inspection of WAM-containing high-magnification EM micrographs showed that when Rrbp1 was silenced, wrappER became less evenly spaced from the mitochondria. More specifically, Rrbp1 silencing caused the wrappER to form "humps" that gave it a wavy appearance (Figure 6D) and, ultimately, increased by ~20% the area of the space between the two organelles ($p < 0.0001$; Figures 6E, S6F, and S6G). Furthermore, it substantially increased the frequency and the total number of wrappER-mitochondria adhesion sites in four of the five mouse livers analyzed (Figure 6F). However, Rrbp1 knockdown did not impact on MAM frequency and ultrastructure (Figures S6H and S6I).

Rrbp1 silencing alters hepatic lipid homeostasis

We leveraged the apparent role of Rrbp1 as a wrappER-mitochondria contacts modifier to investigate whether the wrappER activity in VLDL biogenesis depends on the integrity of its contact with the mitochondria. To this end, we conducted the common VLDL analyses in a large cohort of mice with silenced hepatic Rrbp1 expression. Specifically, we measured neutral lipid and ApoB content in the plasma of control and Rrbp1-silenced mice that were injected with Poloxamer-407 (P407), which blocks VLDL conversion in intermediate-density lipoprotein (IDL) and low-density lipoprotein (LDL) (Wei et al., 2010). This analysis showed that 3 h after P407 injection, plasma neutral lipid and ApoB content was reduced by ~20% in Rrbp1-silenced mice (Figures 7A, 7B, and S7A). Importantly, the lower content of neutral lipids in circulation was not caused by impaired hepatic secretory activity, because plasma proteins and albumin, markers of liver protein synthesis and secretion (Miller et al., 1951), were not affected by Rrbp1 silencing (Figure 7C). Furthermore, immunoblot densitometry analysis showed a parallel reduction in the level of ApoE expression in Rrbp1-silenced liver lysates (Figure 7D). Together, these findings suggest that Rrbp1 silencing reduces VLDL biogenesis rather than the maturation and export of this lipoprotein. Should this be the case, hepatic lipid content would also be expected to be affected by Rrbp1 silencing, because altering VLDL biogenesis redirects the flux of hepatic FFA toward lipid droplet (LD) biogenesis (Kozlitina et al., 2014;

Figure 4. Mouse major urinary proteins (MUPs) are enriched in the wrappER and are predicted to bind palmitic acid

(A) Immunoblot and densitometry analysis of liver WAM fractions (mean ± SD; n = 5 mice; $p < 0.01$ by Mann-Whitney test).

(B) Multiple sequence alignment of all mouse MUP showing the conservation of their ER lumen signal peptide, the eight beta-strands (b1–b8), and the alpha-helix positioned near the C terminus of the protein (α Cterm).

(C) Structural analysis of a representative MUP (1i04). The secondary structure elements are inferred from the structures displayed on the top of the alignment shown in (B).

(D) Structure of the MUP cavity. Residues forming the cavity are predicted using PyMOL; their location is reported at the top of the alignment shown in (B). The left panel shows the measurements of the cavity obtained within the PyMOL framework.

(E) Sequence alignment of the amino acid residues forming the cavity in MUP2, MUP14, and human PTGDS inferred from the structural alignment of MUP1 (1i04) and human PTGDS (3o22), a protein that binds palmitic acid (PA) (Zhou et al., 2010). The sequence alignment shows conservation of the physicochemical properties of the amino acid residues (hydrophobicity conservation) in each cavity (PTGDS and MUP).

(F) Structural prediction assessing the potential binding of a molecule of PA (cyan) in the MUP cavity. The structure of MUP (1i04) is superimposed with PyMOL over that of PTGDS (3o22) with a PA molecule bound in the cavity. The black-labeled residues are the PA-interacting residues of the PTGDS cavity that are identical in the MUP.

(G) Lipidomic analysis showing that WAM-enriched fractions contain more FFA than ER-enriched fractions (n = 10; $p < 0.0001$ by Mann-Whitney test [left]; p values by two-way ANOVA with Bonferroni's post hoc test [right]). CE: cholesterol esters (see Table S4). Means ± SEM are indicated. Data collected from mouse livers at 3 h postprandial.

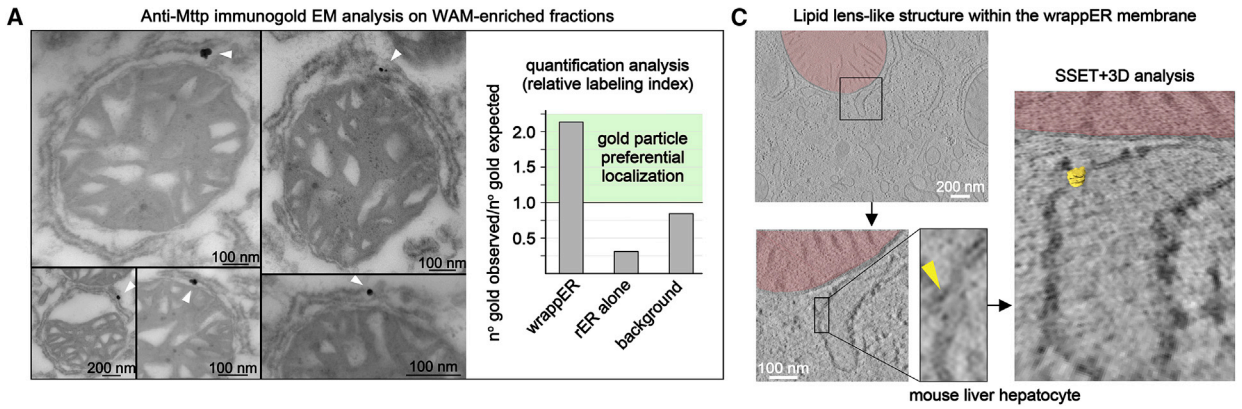

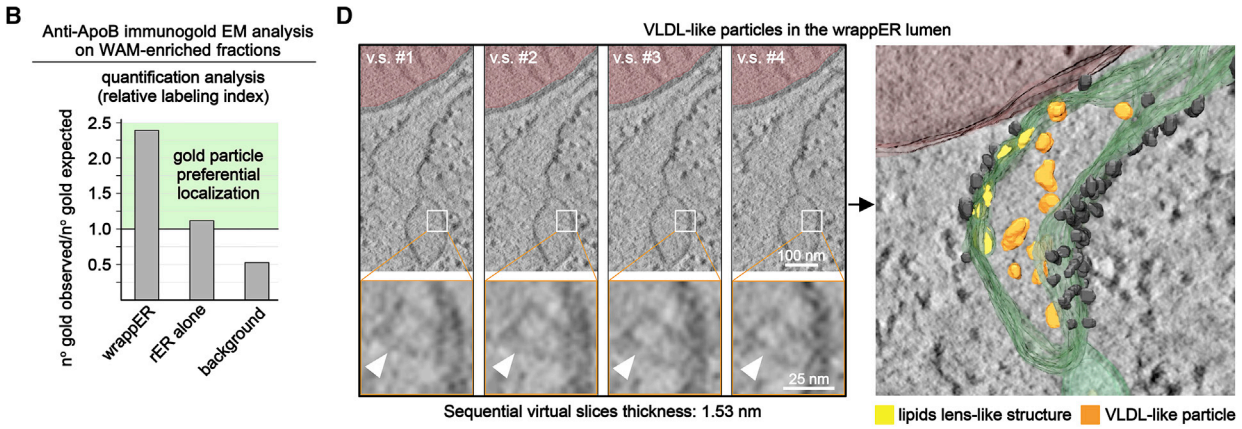

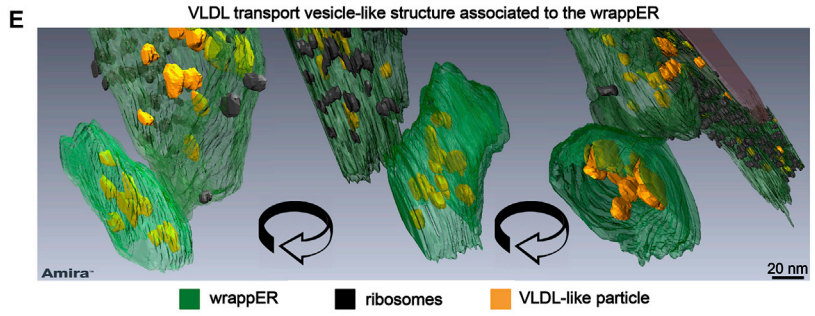

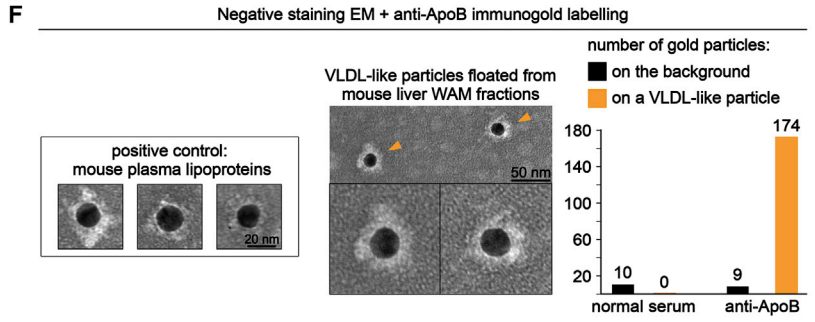

(legend on next page)

Raabe et al., 1999). Indeed, in Rrbp1-silenced livers, we observed a significant increase in hepatic FFA and TAG content (Figures 7E and S7B; Table S5), as well as a considerable increase in LD accumulation and expression of perilipin 2, an LD marker (Figures 7F and S7C). Altogether, these *in vivo* findings functionally link the mechanisms regulating wrappER-mitochondria contacts to intracellular and systemic hepatic lipid homeostasis.

Loss of hepatic VLDL biogenesis modifies wrappER-mitochondria contacts in the liver

To further validate the direct functional relationship between wrappER-mitochondria association and hepatic VLDL synthesis, we sought to test whether the loss of VLDL biogenesis would alter the ultrastructure of this inter-organelle contact. To this end, we performed in-depth 2D-EM morphometric analysis of mouse livers upon acute liver-specific genetic ablation of *Mttp*, the most upstream regulator of VLDL biogenesis (Raabe et al., 1999; Raabe et al., 1998). We injected *Mttp*-floxed mice (Chang et al., 1999) with an AAV8 vector that expresses the Cre recombinase under the control of the liver-specific thyroxine-binding globulin (TBG) promoter (Yan et al., 2012). As expected, three weeks after virus injection, liver expression of Mttp was reduced by more than 90% in every sample tested (Raabe et al., 1999); furthermore, EM and biochemical analysis revealed a robust accumulation of LD and perilipin 2 (Figure 7F). This phenotype was accompanied by ultrastructural remodeling of the wrappER-mitochondria contact (Figures S8A–S8D), with a slight increase in the area of the space that separates the two organelles ($p < 0.01$; Figure S8A) and a nearly 2-fold increase in the number and frequency of adhesion sites ($p < 0.05$; Figure 7G). Overall, the extent of the mitochondrial perimeter occupied by adhesion sites increased by ~44% ($p < 0.001$; Figure 7H). Thus, acute liver-specific ablation of *Mttp* recapitulates the hepatic dyslipidemia phenotype caused by Rrbp1-silencing and promotes a remodeling of the wrappER-mitochondria contact. We conclude that the wrappER-mitochondria contact is a dynamic cellular interface that is integrated in the regulation of hepatic systemic lipid homeostasis.

DISCUSSION

WrappER and mitochondria establish a bona fide inter-organellar contact

Because cells are densely packed with organelles and full of rER sheets, it is essential to ascertain whether the wrappER-mitochondria contact described here is a genuine structural feature as opposed to a nonspecific inter-organellar association formed by crowding, parking, or squashing of the mitochondria against layers of ER membranes. In this work, we employed multiple, independent, and complementary approaches to conclusively demonstrate that the wrappER-mitochondria contact is indeed a bona fide inter-organelle interaction that is functionally linked to the regulation of hepatic lipid homeostasis.

First, we developed a biophysical model to estimate the free energy change associated with the wrapping of a curved ER membrane (wrappER) around a mitochondrion (see energy balance model of the wrappER-mitochondria contact in STAR Methods). Analysis of this model showed that the formation of a wrappER-mitochondria contact is thermodynamically unfavorable due to the high curvature of the wrappER. Thus, the persistent curvature of the wrappER around the mitochondrion during fasting-to-feeding transitions (Figure 1G) has to be maintained either through continuous expenditure of chemical energy, which appears highly unlikely, or through the recruitment of tethering proteins. Without either of these forces at work, the wrappER would either flatten in the "standard" rER-like planar geometry (ER sheet) or assume a vesicle-like structure (see energy balance model of the wrappER-mitochondria contact, in STAR Methods). This conclusion captures the essence of the definition of a contact site as an intracellular domain whose architecture can be maintained only by tethering forces that arise from either protein-protein or protein-lipid interactions (Scorrano et al., 2019). The results of our Rrbp1 silencing experiments (Figures 6D and 6E), which are in agreement with the previous reports showing that this protein tethers rER to mitochondria (Hung et al., 2017), further support this conclusion.

Second, we show that the wrappER-mitochondria contact is dynamic and regulated by the metabolic processes that accompany fasting-to-feeding transitions. This property is compatible with the available data on bona fide inter-organelle contacts that are also dynamic and regulated (Scorrano et al., 2019), often by the nutritional status of the cell. For instance, mitochondria-lysosome contacts in HeLa cells are transient and small (Wong et al., 2018). Conversely, in the mouse liver, LD-mitochondria and MAM contacts tend to be larger and long-lived, but the extent of their inter-organelle association is dynamically regulated by the nutritional status of the animal (Sood et al., 2014; Theurey et al., 2016). Within this context, our study shows that liver wrappER-mitochondria contacts are long-lived but contract by 16% within a few hours from refeeding. This feature is

Figure 5. WrappER is a site of VLDL biogenesis in mouse liver

(A and B) Quantitative immunogold EM analysis performed on WAM-enriched fractions localizes Mttp (A) and ApoB (B) on the wrappER (see Figures S5A and S5B).

(C) Mouse liver SSET+3D analysis showing lipid lens-like structures in the wrappER membrane (Murphy and Vance, 1999; Ohsaki et al., 2008). The yellow arrow indicates the widening of the wrappER phospholipid bilayer (lipid lens, reconstructed in yellow on the right panel; see also Figure S5C).

(D) Mouse liver SSET+3D analysis showing VLDL-like particles in the wrappER lumen. The left panel shows a series of four sequential virtual slices; the high-magnification images at their bottom show a luminal VLDL-like particle (white arrow) (van Antwerpen et al., 1997; Yu et al., 2016). The right panel shows the reconstructed lipid lens (yellow) and VLDL-like particles (orange).

(E) Mouse liver SSET+3D analysis showing a VLDL-transport vesicle-like structure budding from the wrappER (see Video S6).

(F) WAM-enriched fractions enclose ApoB-containing lipoparticles. Images of negative staining anti-ApoB immunogold analysis of lipoproteins floated from mouse plasma (positive control, left panel) and WAM-enriched fractions (central panel). Right: quantification of the data obtained from the experiments performed on WAM fractions ($n = 4$; normal serum [rabbit] was used as negative control).

Data were collected from mouse livers at 3 h postprandial.

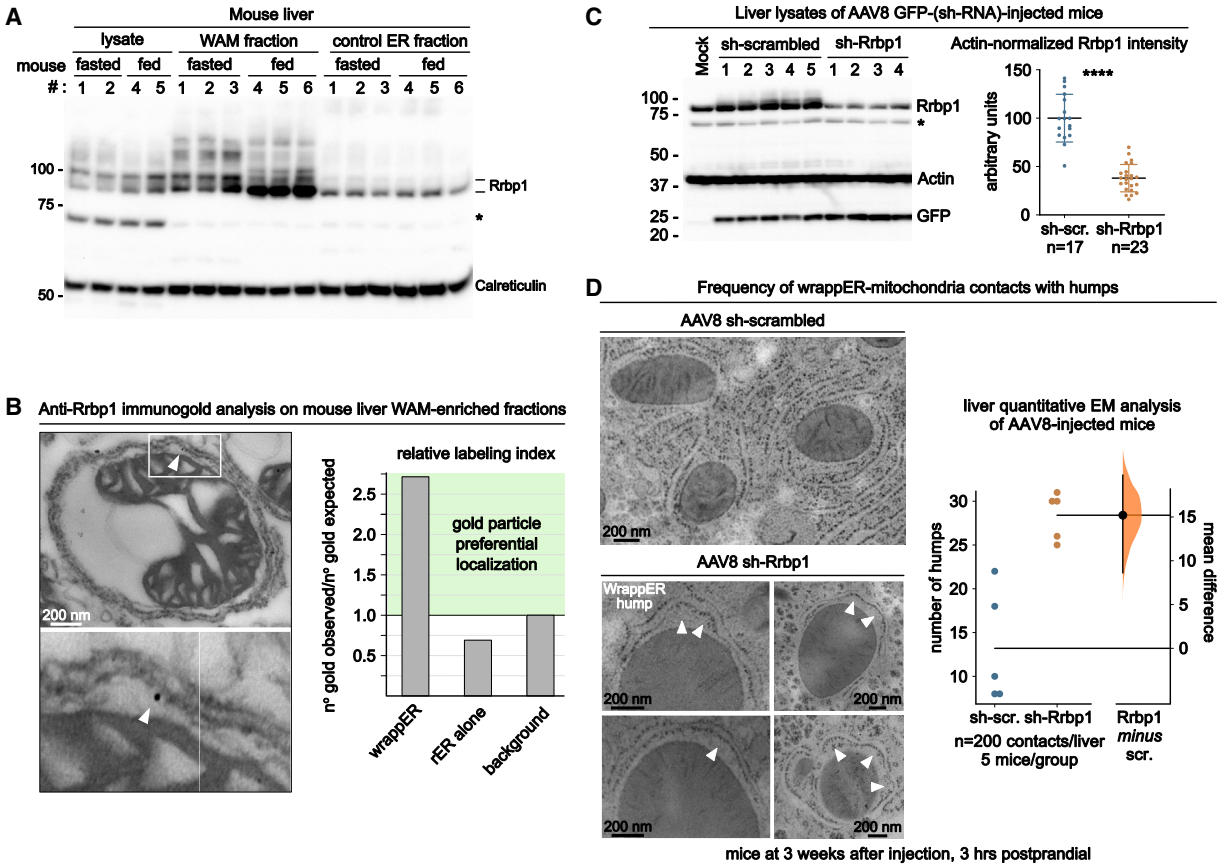

(legend on next page)

particularly important because inter-organelle contact dynamics that are dependent on the nutritional state of the cell are known to be conserved from yeast to mammals (Wang et al., 2014).

Third, the architecture of the wrappER-mitochondria contacts, particularly the uniform, invariant distance between the two organelles during fasting-to-feeding transitions (Figures 1F and 1G), is extremely unlikely to result from fortuitous parking, crowding, or squashing. This conclusion is further supported by our SSET analysis (Videos S1 and S2) showing the absence of other organelles or vesicles, such as endosomes, lysosomes, or Golgi membranes, invariably packed closely around/touching the wrappER. This observation rules out involvement of these organelles in the positioning of the wrappER around the mitochondrion; likewise, it rules out the possibility that the wrappER-mitochondria contact is maintained by the inability of these organelles to move away from each other.

Based on all these converging lines of evidence, we conclude that the wrappER-mitochondria contact described here is a genetically programmed structural parameter of the cell. Whether the wrappER can establish contact with additional cellular organelles remains to be investigated.

Mitochondria motility and dynamics are affected by contacts with the wrappER

In cultured cells, mitochondria continuously move and pass through cycles of fusion and fission, resulting in functional uniformity of the organelle population (Westermann, 2010). However, *in vivo*, mitochondrial fusion and fission are not always balanced, as evidenced by the presence of elongated mitochondria in cardiomyocytes (Ishihara et al., 2015) and fragmented mitochondria in stem cells (Khacho et al., 2016). Similarly, it is likely that the substantial mitochondria trafficking observed in cultured cells (Ahmad et al., 2014; Shen et al., 2018) might not, with the exception of neurons (Takihara et al., 2015), be as frequently present *in vivo* (Wehnekamp et al., 2019). Consistent with these observations, in mouse brown adipose tissue, contacts between mitochondria and LD provide a mechanism to segregate mitochondria into functionally distinct subpopulations that display bioenergetic characteristics and protein composition that are different from those of free, cytosolic mitochondria (Benador et al., 2018). Our present work shows that in the hepatocyte, nearly every mitochondrion establishes extensive and sustained contacts with the wrappER (Figures 1B–1D). These observations imply that mitochondrial mobility in this cell type is limited, a possibility further supported by the extremely low level of expression of transcripts encoding kinesins and other mitochondria-transport proteins in our liver transcriptomic data (Table S2) (Wang and Schwarz, 2009). Should that be the case, mitochondrial fusion should also be reduced, whereas mitochondrial division should not be compromised as it requires interaction with the ER (Friedman et al., 2011). Under this model, the mitochondrial population is expected to be fragmented, that is, dominated by small mitochondria as opposed to elongated ones. Indeed, our previous studies have shown that liver mitochondria are predominantly spherical or oval and are rarely elongated (Sood et al., 2014). In the liver cell, therefore, the ubiquitous diffusion and substantial extension of the wrappER-mitochondria contacts might constitute a means to shift the balance between mitochondrial fusion and division toward the latter, which would confer uniform bioenergetic characteristics to the mitochondrial population.

The MAM ablation phenotype coincides with altered wrappER-mitochondria contacts

Mitofusin-2 (Mfn2) regulates MAM tethering (de Brito and Scorrano, 2008; Naon et al., 2016). In mouse liver, Mfn2 binds PS and can specifically extract PS into membrane domains, favoring PS transfer to mitochondria and mitochondrial PE synthesis. Consequently, hepatic Mfn2 deficiency reduces PS transfer and phospholipid synthesis, leading to ER stress and the development of a NASH-like phenotype and liver cancer (Hernández-Alvarez et al., 2019). The link between phospholipid synthesis and LD accumulation, however, is unknown, suggesting the possibility that the steatosis caused by Mfn2 ablation could be a secondary effect unrelated to MAM activity. Here, we demonstrate that the wrappER provides physical support for MAMs in the liver. In addition, we show that the wrappER has a direct role in the storage of FFAs as well as in their flux as TAGs in the form of VLDL. Therefore, the steatosis caused by Mfn2/MAM ablation might be attributable to altered wrappER-mitochondria contacts instead of a direct effect on phospholipid and calcium transfer (Hernández-Alvarez et al., 2019).

The wrappER as a hub of fatty acid fluxes

High-fructose diets cause gut microbiota to produce excess amounts of acetate that the liver ultimately converts into palmitic acid, which is condensed into TAGs and stored as lipid droplets

Figure 6. Rrbp1 silencing in the mouse liver modifies wrappER-mitochondria contacts

(A) Anti-Rrbp1 immunoblot analysis of WAM- and ER-enriched fractions isolated from livers of fasted (14 h) and fed mice (3 h postprandial). The asterisk denotes an unspecific band of Rrbp1 antibody.

(B) Quantitative anti-Rrbp1 immunogold EM analysis of WAM-enriched fractions (see Figures S6C and S6D).

(C) Anti-Rrbp1 immunoblot and densitometry analyses of liver lysates 3 weeks after injection with AAV8-GFP-sh-Rrbp1 (see Figure S6A). The asterisk denotes an unspecific band of Rrbp1 antibody (n = 17 and 23; mean ± SD; $p < 0.0001$ by Student's t test).

(D) Quantitative EM analysis of control and Rrbp1-silenced livers. Note the "humps" in Rrbp1-silenced samples (white arrows). Right: estimation statistic used to analyze the data; each point represents the frequency of humps measured in each liver analyzed (200 contacts/liver; five livers/group).

(E) Schematic representation of the wrappER-mitochondria contact, with the area of the space separating the organelles depicted in yellow. The central panel plots the data of the area between the organelles in control and Rrbp1-silenced livers (mean; $p < 0.0001$ by Student's t test; 50 wrappER-mitochondria contacts/mouse; five mice/group). The right panel shows their cumulative distribution ($p < 0.0001$ by Kolmogorov-Smirnov test).

(F) Quantitative 2D-EM analysis of wrappER-mitochondria adhesion sites in control and Rrbp1-silenced livers. Data were analyzed by estimation statistics; each point represents the number of observations recorded in each mouse liver analyzed (120 contacts/liver; five livers/group).

Data were collected from mouse livers at 3 h postprandial unless otherwise indicated.

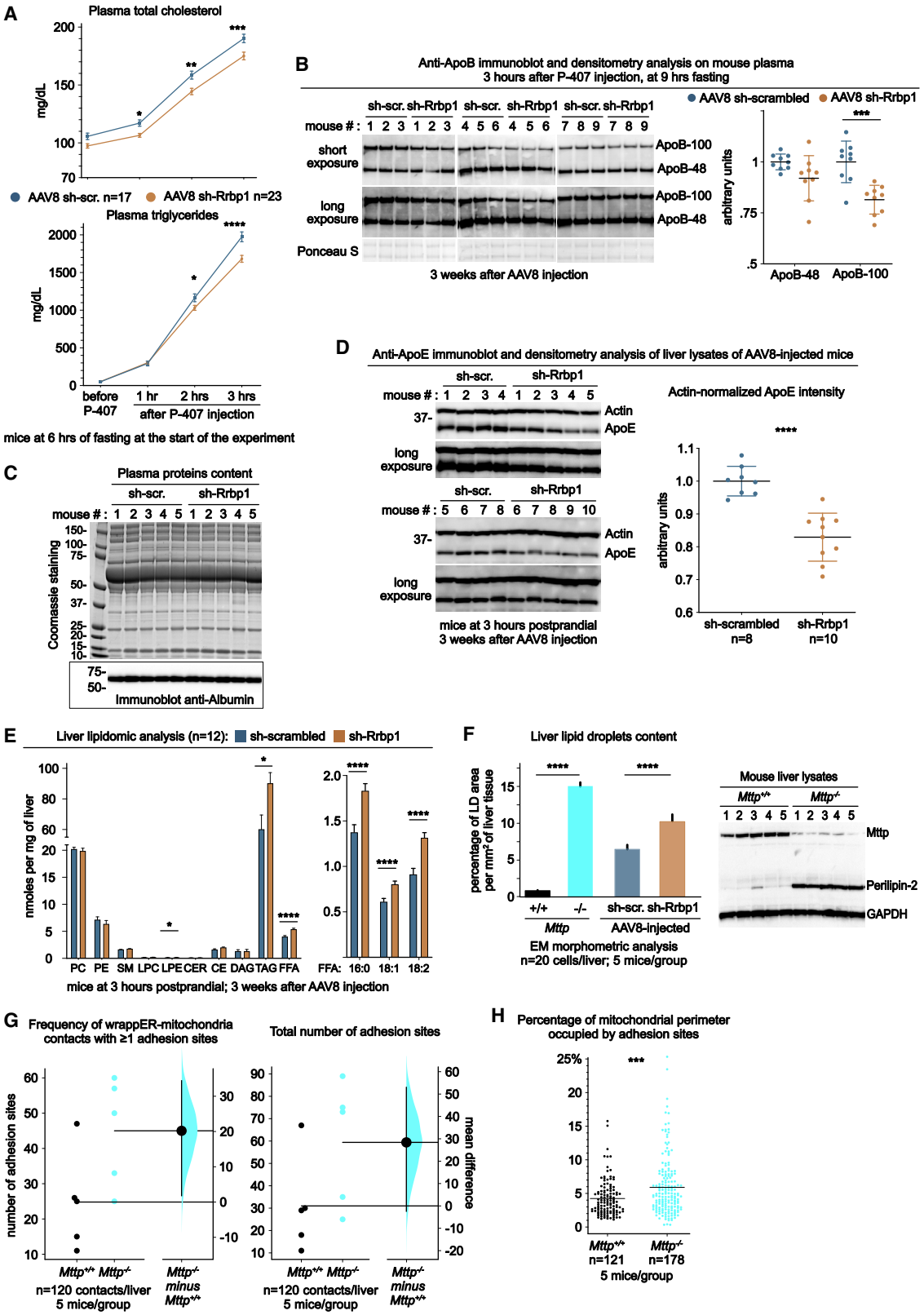

(legend on next page)

(Zhao et al., 2020). The steps that control the flux and storage of palmitic acid within the hepatocyte are not known. However, because the wrappER contains high levels of palmitic acid and palmitic-acid-binding proteins (Figures 4A and 4G), it appears likely that this type of ER plays a role in this pathway. Potentially, the wrappER could control the amount of palmitic acid and its stoichiometric ratio to other FFAs in two ways: (1) by exporting it in a condensed state as VLDL; and (2) by fluxing it into mitochondria, where it can be eliminated through β-oxidation. The adhesion sites between wrappER and mitochondria could be involved in this process, because their number increases in parallel with the level of FFAs present in the hepatic system (Figures 6F and 7E). The data and the WAM protocol provided in this study will help chart the exploration of the role of the wrappER-mitochondria contacts as a hub of intracellular FFA storage and fluxes.

Liver wrappER as a site of VLDL synthesis

The search for the site(s) of VLDL biogenesis has a long history and engendered intense debate in the lipoproteins field. To this date, rER, sER, and MAMs are implicated, individually or in combination, as VLDL synthesis sites (Alexander et al., 1976; Borchardt and Davis, 1987; Borén et al., 1990; Rusiñol et al., 1994). It is not surprising, therefore, that due to this uncertainty, the latest reviews on this subject generically point to the ER as the cradle of the VLDL (Schulze et al., 2019). However, recent advances in electron tomography provided for the demonstration that ER is not a uniform compartment but rather an ensemble of morphologically distinct domains (Carter et al., 2020; Hoffman et al., 2020; Nixon-Abell et al., 2016), each of which will now have to be individually analyzed for their ability to generate VLDL. In this respect, by combining SSET, immunogold EM, and integrated multi-omics analysis, our present work shows that the rER is a bona fide site of VLDL biogenesis and that the wrappER, being a subtype of rER, contributes a limited but substantial share of the VLDL pool that is produced by the liver.

Limitations of study

We analyzed the contribution of Rrbp1 to the wrappER-mitochondria contacts by silencing its expression in the liver using a shRNA-expressing viral vector. Given that this approach only reduced by the expression of Rrbp1 by ~60% (Figure 6C), a caveat of this work is that genetic ablation of *Rrbp1* in the liver is required to validate and extend our observations. Nonetheless, Rrbp1 silencing reveals a therapeutic potential that hardly would be identifiable using a gene-knockout approach. In human patients, short-term administration of an antisense inhibitor of ApoB expression reduces circulating ApoB by 50%, which is similar to the effect of statin, the most common lipid-lowering drug that is prescribed to patients at high risk of coronary disease (Kastelein et al., 2006). Similarly, alirocumab, a monoclonal antibody directed against PCSK9, decreases plasma LDL cholesterol and ApoB by ~47% (Reyes-Soffer et al., 2017), substantially reducing the risk of recurrent ischemic cardiovascular events in patients with a history of acute coronary syndrome (Schwartz et al., 2018). An open question, therefore, is whether the 20% reduction in the ApoB-100 secretion caused by Rrbp1 knockdown (Figure 7B) could suffice to consider wrappER-mitochondria contact modifiers as potential lipid-lowering therapeutics.

Due to the large number of mice that was required to complete this work, only one age/sex group was used (males, aged 3–4 months). Therefore, because sex and age are major biological variables, a limitation of this work is that the potential effects of these factors on some of our conclusions are not addressed. In particular, this pertains to the extent and dynamics of the wrappER-mitochondria contacts during fasting/feeding transitions, which are known to be controlled pathways that are profoundly influenced by the age and sex of the animal, such as mTORC1 (Baar et al., 2016; Liu and Sabatini, 2020). These limitations notwithstanding, the present study merges existing concepts in lipoprotein biology with the principles and paradigms of current cell biology to introduce the notion that inter-organellar contacts are an integral component of the mechanisms that regulate VLDL output *in vivo*.

Figure 7. WrappER-mitochondria contacts are integrated in hepatic systemic lipid homeostasis

(A) Silencing of Rrbp1 in the liver lowers hepatic TAGs and total cholesterol secretion in the bloodstream. The panels show mean ± SEM of the values of total cholesterol (top) and TAGs (bottom) measured in the plasma of mice injected with Poloxamer-407 (Brenachot et al., 2017; Huang et al., 2018; Marshall et al., 2014; Millar et al., 2005; see Figure S7A; p values by two-way ANOVA with Bonferroni's post hoc test).

(B) Immunoblot and densitometry analysis of ApoB expression in the plasma of control mice and mice with silenced Rrbp1 expression in the liver (mean ± SD, n = 9; p values by two-way ANOVA with Bonferroni's post hoc test).

(C) Anti-albumin immunoblot analysis and electrophoretic analysis of the proteins present in the plasma of control mice and mice with silenced Rrbp1 expression. The two groups of animals have similar liver function and secretion activity.

(D) Anti-ApoE immunoblot and densitometry analysis of control and Rrbp1-silenced mouse liver lysates (mean ± SD; n = 8 and 10; $p < 0.0001$ by Mann-Whitney test; 20 μg/lane).

(E) Liver lipidomic analysis. Rrbp1 silencing in the liver increases the content of hepatic TAGs and FFA (mean ± SEM; n = 12; p values by Mann-Whitney test [left] and two-way ANOVA with Bonferroni's post hoc test [right]). Only the most abundant FFA species are shown in the right panel (see Table S5). PC, phosphatidylcholine; PE, phosphatidylethanolamine; SM, sphingomyelin; LPC, lysophosphatidylcholine; LPE, lysophosphatidylethanolamine; CER, ceramide; CE, cholesteryl ester; DAG, diacylglycerol.

(F) EM analysis showing LDs accumulation in Rrbp1-silenced and $Mttp^{-/-}$ livers ($p < 0.0001$ by Student's t test; 20 hepatocytes/liver; five mice/group). The immunoblot shows a parallel expression of perilipin 2, marker for LD (see Figure S7C).

(G) EM analysis showing that acute hepatic ablation of *Mttp* increases the frequency (left) and total number (right) of wrappER-mitochondria adhesion sites. Data were analyzed by estimation statistics; each point represents the number of observations recorded in each mouse liver analyzed (120 contacts/liver; five livers/group).

(H) EM analysis showing an increase in the size of wrappER-mitochondria adhesion sites in $Mttp^{-/-}$ livers (mean; $p < 0.001$ by Student's t test). The value of each point measures the length of an adhesion site normalized for the length of the mitochondrial perimeter on which it rests (n = 5 mice/group).

Data shown in (D) and (H) were collected from the mouse livers at 3 h postprandial.

STAR★METHODS

Detailed methods are provided in the online version of this paper and include the following:

- KEY RESOURCES TABLE
- RESOURCE AVAILABILITY
  - Lead contact
  - Materials availability
  - Data and code availability
- EXPERIMENTAL MODEL AND SUBJECT DETAILS
- METHOD DETAILS
  - Energy balance model of the wrappER-mitochondria contact
  - Blood plasma collection and *in vivo* VLDL secretion analysis
  - Immunoblot analysis
  - Preparation of cellular fractions enriched in wrappER-associated mitochondria from the mouse liver
  - WAM-enriched fraction fixation and embedding for electron microscopy
  - Tissue sample preparation for EM analysis, ET imaging and 3D reconstruction
  - Lipoproteins imaging by negative staining and immunogold EM analysis
  - Pre-embedding immunogold EM analysis on WAM-enriched fractions
  - Immunohistochemistry
  - RNA isolation and sequencing
  - Protein mass spectrometry analysis
  - Lipidomic analysis
  - MAM activity assay
  - AAV8-Shrna design and *in vivo* delivery
  - Inactivation of Mttp with Cre adenovirus in the liver
  - MUP bioinformatic analysis
  - Data reporting
- QUANTIFICATION AND STATISTICAL ANALYSIS

SUPPLEMENTAL INFORMATION

Supplemental information can be found online at https://doi.org/10.1016/j.celrep.2021.108873.

ACKNOWLEDGMENTS

We thank Lawrence C.B. Chan (Baylor College of Medicine) and Mahmood M. Hussein (NYU Langone hospital) for the *Mttp*-floxed mice and valuable discussions; S. Bourassa, M. Dumont, and C. Joly-Beauparlant (CHU, Quebec) for support with protein mass spectrometry (MS) and RNA-sequencing analysis; J.C. Savage for providing the focused ion beam scanning electron microscopy dataset; Leonardo Pellegrini for SSET+3D reconstruction; R. Watts (University of Alberta) for technical assistance; and Serge Rivest (CHU, Quebec) for supporting the early phase of this study.

I.A. and N.I. are recipients of PhD scholarships from the Centre Thématique de Recherche en Neurosciences (CTRN) and Fonds de la recherche en sante du Quebec (FRQS). This study was funded by grants from the CIHR (201603PJT-365052) and NSERC (RGPIN-2017-06130) to L.P. M.G. is supported by CARIPARO (starting grant 2016 AIFbiol) and UniPD (Stars program); R.L. is supported by CIHR (201709PJT-156314) and NSERC (RGPIN-2017-04734); M.J.M. is supported by the NSF (DMS-1716114); K.T. is supported by CIHR (MOP-81142); T.Q.d.A.V. is supported by the NIH (HL122677 and DK112119); and E.V.K. is supported by intramural funds from the NCBI of the NIH.

AUTHOR CONTRIBUTIONS

I.A. and N.I. designed and performed experiments, analyzed data, and wrote the manuscript; A.R. and P.L. contributed SSET and EM data; R.G.-A., F.C., G.V., M.G., and R.L. provided technical expertise, reagents, and discussions; M.J.M. contributed the biophysical modeling; K.J.W. and T.Q.d.A.V. contributed lipidomic data and analysis; G.F., S.L.M., and E.V.K. contributed bioinformatic analysis; K.T., L.S., and E.V.K. analyzed data and participated in writing the manuscript; and L.P. conceived the study, analyzed data, supervised the study, and wrote the manuscript.

DECLARATION OF INTERESTS

The authors declare no competing interests.

Received: October 12, 2020
Revised: December 18, 2020
Accepted: February 23, 2021
Published: March 16, 2021

REFERENCES

Ahmad, T., Mukherjee, S., Pattnaik, B., Kumar, M., Singh, S., Kumar, M., Rehman, R., Tiwari, B.K., Jha, K.A., Barhanpurkar, A.P., et al. (2014). Miro1 regulates intercellular mitochondrial transport & enhances mesenchymal stem cell rescue efficacy. EMBO J. *33*, 994–1010.

Alexander, C.A., Hamilton, R.L., and Havel, R.J. (1976). Subcellular localization of B apoprotein of plasma lipoproteins in rat liver. J. Cell Biol. *69*, 241–263.

Arendt, D. (2008). The evolution of cell types in animals: emerging principles from molecular studies. Nat. Rev. Genet. *9*, 868–882.

Arnold, L., Perrin, H., de Chanville, C.B., Saclier, M., Hermand, P., Poupel, L., Guyon, E., Licata, F., Carpentier, W., Vilar, J., et al. (2015). CX3CR1 deficiency promotes muscle repair and regeneration by enhancing macrophage ApoE production. Nat. Commun. *6*, 8972.

Arruda, A.P., Pers, B.M., Parlakgül, G., Güney, E., Inouye, K., and Hotamisligil, G.S. (2014). Chronic enrichment of hepatic endoplasmic reticulum-mitochondria contact leads to mitochondrial dysfunction in obesity. Nat. Med. *20*, 1427–1435.

Baar, E.L., Carbajal, K.A., Ong, I.M., and Lamming, D.W. (2016). Sex- and tissue-specific changes in mTOR signaling with age in C57BL/6J mice. Aging Cell *15*, 155–166.

Bayraktar, E.C., Baudrier, L., Özerdem, C., Lewis, C.A., Chan, S.H., Kunchok, T., Abu-Remaileh, M., Cangelosi, A.L., Sabatini, D.M., Birsoy, K., and Chen, W.W. (2019). MITO-Tag Mice enable rapid isolation and multimodal profiling of mitochondria from specific cell types in vivo. Proc. Natl. Acad. Sci. USA *116*, 303–312.

Becker, L., Gharib, S.A., Irwin, A.D., Wijsman, E., Vaisar, T., Oram, J.F., and Heinecke, J.W. (2010). A macrophage sterol-responsive network linked to atherogenesis. Cell Metab. *11*, 125–135.

Benador, I.Y., Veliova, M., Mahdaviani, K., Petcherski, A., Wikstrom, J.D., Assali, E., Acin-Pérez, R., Shum, M., Oliveira, M.F., Cinti, S., et al. (2018). Mitochondria Bound to Lipid Droplets Have Unique Composition, Bioenergetics, and Dynamics That Support Lipid Droplet Expansion. Cell Metab. *27*, 869–885.

Bernard, C. (2019). Changing the way we report, interpret, and discuss our results to rebuild trust in our research. eNeuro *6*, 4–6.

Bernhard, W., and Rouiller, C. (1956). Close topographical relationship between mitochondria and ergastoplasm of liver cells in a definite phase of cellular activity. J. Biophys. Biochem. Cytol. *2 (4, Suppl)*, 73–78.

Bligh, E.G., and Dyer, W.J. (1959). A rapid method of total lipid extraction and purification. Can. J. Biochem. Physiol. *37*, 911–917.

Borchardt, R.A., and Davis, R.A. (1987). Intrahepatic assembly of very low density lipoproteins. Rate of transport out of the endoplasmic reticulum determines rate of secretion. J. Biol. Chem. *262*, 16394–16402.

Borén, J., Wettesten, M., Sjöberg, A., Thorlin, T., Bondjers, G., Wiklund, O., and Olofsson, S.-O. (1990). The assembly and secretion of apoB 100 containing lipoproteins in Hep G2 cells. Evidence for different sites for protein synthesis and lipoprotein assembly. J. Biol. Chem. *265*, 10556–10564.

Bray, N.L., Pimentel, H., Melsted, P., and Pachter, L. (2016). Near-optimal probabilistic RNA-seq quantification. Nat. Biotechnol. *34*, 525–527.

Brenachot, X., Gautier, T., Nédélec, E., Deckert, V., Laderrière, A., Nuzzaci, D., Rigault, C., Lemoine, A., Pénicaud, L., Lagrost, L., and Benani, A. (2017). Brain control of plasma cholesterol involves polysialic acid molecules in the hypothalamus. Front. Neurosci. *11*, 245.

Campelo, F., van Galen, J., Turacchio, G., Parashuraman, S., Kozlov, M.M., García-Parajo, M.F., and Malhotra, V. (2017). Sphingomyelin metabolism controls the shape and function of the Golgi cisternae. eLife *6*, 1–40.

Carter, S.D., Hampton, C.M., Langlois, R., Melero, R., Farino, Z.J., Calderon, M.J., Li, W., Wallace, C.T., Tran, N.H., Grassucci, R.A., et al. (2020). Ribosome-associated vesicles: A dynamic subcompartment of the endoplasmic reticulum in secretory cells. Sci. Adv. *6*, eaay9572.

Chang, B.H.J., Liao, W., Li, L., Nakamuta, M., Mack, D., and Chan, L. (1999). Liver-specific inactivation of the abetalipoproteinemia gene completely abrogates very low density lipoprotein/low density lipoprotein production in a viable conditional knockout mouse. J. Biol. Chem. *274*, 6051–6055.

Chang, C.L., Weigel, A.V., Ioannou, M.S., Pasolli, H.A., Xu, C.S., Peale, D.R., Shtengel, G., Freeman, M., Hess, H.F., Blackstone, C., and Lippincott-Schwartz, J. (2019). Spastin tethers lipid droplets to peroxisomes and directs fatty acid trafficking through ESCRT-III. J. Cell Biol. *218*, 2583–2599.

Chen, S., Zhou, Y., Chen, Y., and Gu, J. (2018). fastp: an ultra-fast all-in-one FASTQ preprocessor. Bioinformatics *34*, i884–i890.

Chu, B.B., Liao, Y.C., Qi, W., Xie, C., Du, X., Wang, J., Yang, H., Miao, H.H., Li, B.L., and Song, B.L. (2015). Cholesterol transport through lysosome-peroxisome membrane contacts. Cell *161*, 291–306.

Csordás, G., Renken, C., Várnai, P., Walter, L., Weaver, D., Buttle, K.F., Balla, T., Mannella, C.A., and Hajnóczky, G. (2006). Structural and functional features and significance of the physical linkage between ER and mitochondria. J. Cell Biol. *174*, 915–921.

Dash, S., Xiao, C., Morgantini, C., and Lewis, G.F. (2015). New Insights into the Regulation of Chylomicron Production. Annu. Rev. Nutr. *35*, 265–294.

de Brito, O.M., and Scorrano, L. (2008). Mitofusin 2 tethers endoplasmic reticulum to mitochondria. Nature *456*, 605–610.

Di Paolo, G., and De Camilli, P. (2006). Phosphoinositides in cell regulation and membrane dynamics. Nature *443*, 651–657.

Dong, R., Saheki, Y., Swarup, S., Lucast, L., Harper, J.W., and De Camilli, P. (2016). Endosome-ER Contacts Control Actin Nucleation and Retromer Function through VAP-Dependent Regulation of PI4P. Cell *166*, 408–423.

Edgar, R.C. (2004). MUSCLE: multiple sequence alignment with high accuracy and high throughput. Nucleic Acids Res. *32*, 1792–1797.

Ewels, P., Magnusson, M., Lundin, S., and Käller, M. (2016). MultiQC: summarize analysis results for multiple tools and samples in a single report. Bioinformatics *32*, 3047–3048.

Franke, W.W., and Kartenbeck, J. (1971). Outer mitochondrial membrane continuous with endoplasmic reticulum. Protoplasma *73*, 35–41.

Friedman, J.R., Lackner, L.L., West, M., DiBenedetto, J.R., Nunnari, J., and Voeltz, G.K. (2011). ER Tubules Mark Sites of Mitochondrial Division. Science *334*, 358–362.

Fu, S., Watkins, S.M., and Hotamisligil, G.S. (2012). The role of endoplasmic reticulum in hepatic lipid homeostasis and stress signaling. Cell Metab. *15*, 623–634.

Galluzzi, L., Yamazaki, T., and Kroemer, G. (2018). Linking cellular stress responses to systemic homeostasis. Nat. Rev. Mol. Cell Biol. *19*, 731–745.

Garewal, M., Zhang, L., and Ren, G. (2013). Optimized Negative-Staining Protocol for Examining Lipid-Protein Interactions by Electron Microscopy. Methods Mol. Biol. *2019*, 163–173.

Giacomello, M., and Pellegrini, L. (2016). The coming of age of the mitochondria-ER contact: a matter of thickness. Cell Death Differ. *23*, 1417–1427.

Gilchrist, A., Au, C.E., Hiding, J., Bell, A.W., Fernandez-Rodriguez, J., Lesimple, S., Nagaya, H., Roy, L., Gosline, S.J.C., Hallett, M., et al. (2006). Quantitative proteomics analysis of the secretory pathway. Cell *127*, 1265–1281.

Goldstein, J.L., and Brown, M.S. (2015). A century of cholesterol and coronaries: from plaques to genes to statins. Cell *161*, 161–172.

Helfrich, W. (1973). Elastic properties of lipid bilayers: theory and possible experiments. Z. Naturforsch. C *28*, 693–703.

Hernández-Alvarez, M.I., Sebastián, D., Vives, S., Ivanova, S., Bartoccioni, P., Kakimoto, P., Plana, N., Veiga, S.R., Hernández, V., Vasconcelos, N., et al. (2019). Deficient Endoplasmic Reticulum-Mitochondrial Phosphatidylserine Transfer Causes Liver Disease. Cell *177*, 881–895.e17.

Ho, J., Tumkaya, T., Aryal, S., Choi, H., and Claridge-Chang, A. (2019). Moving beyond P values: data analysis with estimation graphics. Nat. Methods *16*, 565–566.

Hoffman, D.P., Shtengel, G., Xu, C.S., Campbell, K.R., Freeman, M., Wang, L., Milkie, D.E., Pasolli, H.A., Iyer, N., Bogovic, J.A., et al. (2020). Correlative three-dimensional super-resolution and block-face electron microscopy of whole vitreously frozen cells. Science *367*, eaaz5357.

Höglinger, D., Burgoyne, T., Sanchez-Heras, E., Hartwig, P., Colaco, A., Newton, J., Futter, C.E., Spiegel, S., Platt, F.M., and Eden, E.R. (2019). NPC1 regulates ER contacts with endocytic organelles to mediate cholesterol egress. Nat. Commun. *10*, 4276.

Hu, M., Briguglio, J.J., and Deserno, M. (2012). Determining the Gaussian curvature modulus of lipid membranes in simulations. Biophys. J. *102*, 1403–1410.

Huang, H., Lee, S.H., Sousa-Lima, I., Kim, S.S., Hwang, W.M., Dagon, Y., Yang, W.M., Cho, S., Kang, M.C., Seo, J.A., et al. (2018). Rho-kinase/AMPK axis regulates hepatic lipogenesis during overnutrition. J. Clin. Invest. *128*, 5335–5350.

Hung, V., Lam, S.S., Udeshi, N.D., Svinkina, T., Guzman, G., Mootha, V.K., Carr, S.A., and Ting, A.Y. (2017). Proteomic mapping of cytosol-facing outer mitochondrial and ER membranes in living human cells by proximity biotinylation. eLife *6*, 6.

Hussain, M.M. (2000). A proposed model for the assembly of chylomicrons. Atherosclerosis *148*, 1–15.

Ishihara, T., Ban-Ishihara, R., Maeda, M., Matsunaga, Y., Ichimura, A., Kyogoku, S., Aoki, H., Katada, S., Nakada, K., Nomura, M., et al. (2015). Dynamics of mitochondrial DNA nucleoids regulated by mitochondrial fission is essential for maintenance of homogeneously active mitochondria during neonatal heart development. Mol. Cell. Biol. *35*, 211–223.

Israelachvili, J. (2011). Intermolecular and Surface Forces (Elsevier).

Janson, G., Zhang, C., Prado, M.G., and Paiardini, A. (2017). PyMod 2.0: improvements in protein sequence-structure analysis and homology modeling within PyMOL. Bioinformatics *33*, 444–446.

Kastelein, J.J.P., Wedel, M.K., Baker, B.F., Su, J., Bradley, J.D., Yu, R.Z., Chuang, E., Graham, M.J., and Crooke, R.M. (2006). Potent reduction of apolipoprotein B and low-density lipoprotein cholesterol by short-term administration of an antisense inhibitor of apolipoprotein B. Circulation *114*, 1729–1735.

Khacho, M., Clark, A., Svoboda, D.S., Azzi, J., MacLaurin, J.G., Meghaizel, C., Sesaki, H., Lagace, D.C., Germain, M., Harper, M.E., et al. (2016). Mitochondrial Dynamics Impacts Stem Cell Identity and Fate Decisions by Regulating a Nuclear Transcriptional Program. Cell Stem Cell *19*, 232–247.

Kim, Y.J., Lee, M.C., Kim, S.J., and Chun, J.Y. (2000). Identification and characterization of multiple isoforms of a mouse ribosome receptor. Gene *261*, 337–344.

Knorr, R.L., Dimova, R., and Lipowsky, R. (2012). Curvature of double-membrane organelles generated by changes in membrane size and composition. PLoS ONE *7*, e32753.

Kozlitina, J., Smagris, E., Stender, S., Nordestgaard, B.G., Zhou, H.H., Tybjærg-Hansen, A., Vogt, T.F., Hobbs, H.H., and Cohen, J.C. (2014). Exome-wide association study identifies a TM6SF2 variant that confers susceptibility to nonalcoholic fatty liver disease. Nat. Genet. *46*, 352–356.

Langley, R., Leung, E., Morris, C., Berg, R., McDonald, M., Weaver, A., Parry, D.A., Ni, J., Su, J., Gentz, R., et al. (1998). Identification of multiple forms of 180-kDa ribosome receptor in human cells. DNA Cell Biol. *17*, 449–460.

Lee, J.E., Cathey, P.I., Wu, H., Parker, R., and Voeltz, G.K. (2020). Endoplasmic reticulum contact sites regulate the dynamics of membraneless organelles. Science *367*, eaay7108.

Lipowsky, R. (1991). The conformation of membranes. Nature *349*, 475–481.

Liu, G.Y., and Sabatini, D.M. (2020). mTOR at the nexus of nutrition, growth, ageing and disease. Nat. Rev. Mol. Cell Biol. *21*, 183–203.

Lu, Z., Szafron, D., Greiner, R., Lu, P., Wishart, D.S., Poulin, B., Anvik, J., Macdonell, C., and Eisner, R. (2004). Predicting subcellular localization of proteins using machine-learned classifiers. Bioinformatics *20*, 547–556.

Marshall, S.M., Kelley, K.L., Davis, M.A., Wilson, M.D., McDaniel, A.L., Lee, R.G., Crooke, R.M., Graham, M.J., Rudel, L.L., Brown, J.M., and Temel, R.E. (2014). Reduction of VLDL secretion decreases cholesterol excretion in niemann-pick C1-like 1 hepatic transgenic mice. PLoS ONE *9*, e84418.

Mastronarde, D.N. (1997). Dual-axis tomography: an approach with alignment methods that preserve resolution. J. Struct. Biol. *120*, 343–352.

Mayhew, T.M., Lucocq, J.M., and Griffiths, G. (2002). Relative labelling index: a novel stereological approach to test for non-random immunogold labelling of organelles and membranes on transmission electron microscopy thin sections. J. Microsc. *205*, 153–164.

McMahon, H.T., and Gallop, J.L. (2005). Membrane curvature and mechanisms of dynamic cell membrane remodelling. Nature *438*, 590–596.

Millar, J.S., Cromley, D.A., McCoy, M.G., Rader, D.J., and Billheimer, J.T. (2005). Determining hepatic triglyceride production in mice: comparison of poloxamer 407 with Triton WR-1339. J. Lipid Res. *46*, 2023–2028.

Miller, L.L., Bly, C.G., Watson, M.L., and Bale, W.F. (1951). The dominant role of the liver in plasma protein synthesis; a direct study of the isolated perfused rat liver with the aid of lysine-epsilon-C14. J. Exp. Med. *94*, 431–453.

Montisano, D.F., Cascarano, J., Pickett, C.B., and James, T.W. (1982). Association between mitochondria and rough endoplasmic reticulum in rat liver. Anat. Rec. *203*, 441–450.

Murphy, D.J., and Vance, J. (1999). Mechanisms of lipid-body formation. Trends Biochem. Sci. *24*, 109–115.

Naon, D., Zaninello, M., Giacomello, M., Varanita, T., Grespi, F., Lakshminaranayan, S., Serafini, A., Semenzato, M., Herkenne, S., Hernández-Alvarez, M.I., et al. (2016). Critical reappraisal confirms that Mitofusin 2 is an endoplasmic reticulum-mitochondria tether. Proc. Natl. Acad. Sci. USA *113*, 11249–11254.

Nesvizhskii, A.I., Keller, A., Kolker, E., and Aebersold, R. (2003). A statistical model for identifying proteins by tandem mass spectrometry. Anal. Chem. *75*, 4646–4658.

Nixon-Abell, J., Obara, C.J., Weigel, A.V., Li, D., Legant, W.R., Xu, C.S., Pasolli, H.A., Harvey, K., Hess, H.F., Betzig, E., et al. (2016). Increased spatiotemporal resolution reveals highly dynamic dense tubular matrices in the peripheral ER. Science *354*, aaf3928.

Ohsaki, Y., Cheng, J., Suzuki, M., Fujita, A., and Fujimoto, T. (2008). Lipid droplets are arrested in the ER membrane by tight binding of lipidated apolipoprotein B-100. J. Cell Sci. *121*, 2415–2422.

Price, M.N., Dehal, P.S., and Arkin, A.P. (2010). FastTree 2–approximately maximum-likelihood trees for large alignments. PLoS ONE *5*, e9490.

Raabe, M., Flynn, L.M., Zlot, C.H., Wong, J.S., Véniant, M.M., Hamilton, R.L., and Young, S.G. (1998). Knockout of the abetalipoproteinemia gene in mice: reduced lipoprotein secretion in heterozygotes and embryonic lethality in homozygotes. Proc. Natl. Acad. Sci. USA *95*, 8686–8691.

Raabe, M., Véniant, M.M., Sullivan, M.A., Zlot, C.H., Björkegren, J., Nielsen, L.B., Wong, J.S., Hamilton, R.L., and Young, S.G. (1999). Analysis of the role of microsomal triglyceride transfer protein in the liver of tissue-specific knockout mice. J. Clin. Invest. *103*, 1287–1298.

Reyes-Soffer, G., Pavlyha, M., Ngai, C., Thomas, T., Holleran, S., Ramakrishnan, R., Karmally, W., Nandakumar, R., Fontanez, N., Obunike, J., et al. (2017). Effects of PCSK9 inhibition with alirocumab on lipoprotein metabolism in healthy humans. Circulation *135*, 352–362.

Rizzuto, R., Pinton, P., Carrington, W., Fay, F.S., Fogarty, K.E., Lifshitz, L.M., Tuft, R.A., and Pozzan, T. (1998). Close contacts with the endoplasmic reticulum as determinants of mitochondrial Ca2+ responses. Science *280*, 1763–1766.

Rusiñol, A.E., Cui, Z., Chen, M.H., and Vance, J.E. (1994). A unique mitochondria-associated membrane fraction from rat liver has a high capacity for lipid synthesis and contains pre-Golgi secretory proteins including nascent lipoproteins. J. Biol. Chem. *269*, 27494–27502.

Sandhu, J., Li, S., Fairall, L., Pfisterer, S.G., Gurnett, J.E., Xiao, X., Weston, T.A., Vashi, D., Ferrari, A., Orozco, J.L., et al. (2018). Aster Proteins Facilitate Nonvesicular Plasma Membrane to ER Cholesterol Transport in Mammalian Cells. Cell *175*, 514–529.e20.

Schulze, R.J., Schott, M.B., Casey, C.A., Tuma, P.L., and McNiven, M.A. (2019). The cell biology of the hepatocyte: A membrane trafficking machine. J. Cell Biol. *218*, 2096–2112.

Schwartz, G.G., Steg, P.G., Szarek, M., Bhatt, D.L., Bittner, V.A., Diaz, R., Edelberg, J.M., Goodman, S.G., Hanotin, C., Harrington, R.A., et al.; ODYSSEY OUTCOMES Committees and Investigators (2018). Alirocumab and Cardiovascular Outcomes after Acute Coronary Syndrome. N. Engl. J. Med. *379*, 2097–2107.

Scorrano, L., De Matteis, M.A., Emr, S., Giordano, F., Hajnóczky, G., Kornmann, B., Lackner, L.L., Levine, T.P., Pellegrini, L., Reinisch, K., et al. (2019). Coming together to define membrane contact sites. Nat. Commun. *10*, 1287.

Seifert, U. (1997). Configurations of fluid membranes and vesicles. Adv. Phys. *46*, 13–137.

Shelness, G.S., and Sellers, J.A. (2001). Very-low-density lipoprotein assembly and secretion. Curr. Opin. Lipidol. *12*, 151–157.

Shelness, G.S., Ingram, M.F., Huang, X.F., and DeLozier, J.A. (1999). Apolipoprotein B in the rough endoplasmic reticulum: translation, translocation and the initiation of lipoprotein assembly. J. Nutr. *129* (*2S, Suppl*), 456S–462S.

Shen, J., Zhang, J.H., Xiao, H., Wu, J.M., He, K.M., Lv, Z.Z., Li, Z.J., Xu, M., and Zhang, Y.Y. (2018). Mitochondria are transported along microtubules in membrane nanotubes to rescue distressed cardiomyocytes from apoptosis article. Cell Death Dis. *9*, 81.

Sheng, Z.H., and Cai, Q. (2012). Mitochondrial transport in neurons: impact on synaptic homeostasis and neurodegeneration. Nat. Rev. Neurosci. *13*, 77–93.

Shiao, Y.J., Balcerzak, B., and Vance, J.E. (1998). A mitochondrial membrane protein is required for translocation of phosphatidylserine from mitochondria-associated membranes to mitochondria. Biochem. J. *331*, 217–223.

Siddiqi, S.A. (2008). VLDL exits from the endoplasmic reticulum in a specialized vesicle, the VLDL transport vesicle, in rat primary hepatocytes. Biochem. J. *413*, 333–342.

Sood, A., Jeyaraju, D.V., Prudent, J., Caron, A., Lemieux, P., McBride, H.M., Laplante, M., Tóth, K., and Pellegrini, L. (2014). A Mitofusin-2-dependent inactivating cleavage of Opa1 links changes in mitochondria cristae and ER contacts in the postprandial liver. Proc. Natl. Acad. Sci. USA *111*, 16017–16022.

Steinkühler, J., Knorr, R.L., Zhao, Z., Bhatia, T., Bartelt, S.M., Wegner, S., Dimova, R., and Lipowsky, R. (2020). Controlled division of cell-sized vesicles by low densities of membrane-bound proteins. Nat. Commun. *11*, 905.

Syed, G.H., Khan, M., Yang, S., and Siddiqui, A. (2017). Hepatitis C Virus Lipoviroparticles Assemble in the Endoplasmic Reticulum (ER) and Bud off from the ER to the Golgi Compartment in COPII Vesicles. J. Virol. *91*, e00499–e17.

Takihara, Y., Inatani, M., Eto, K., Inoue, T., Kreymerman, A., Miyake, S., Ueno, S., Nagaya, M., Nakanishi, A., Iwao, K., et al. (2015). In vivo imaging of axonal transport of mitochondria in the diseased and aged mammalian CNS. Proc. Natl. Acad. Sci. USA *112*, 10515–10520.

Theurey, P., Tubbs, E., Vial, G., Jacquemetton, J., Bendridi, N., Chauvin, M.A., Alam, M.R., Le Romancer, M., Vidal, H., and Rieusset, J. (2016). Mitochondria-associated endoplasmic reticulum membranes allow adaptation of mitochondrial metabolism to glucose availability in the liver. J. Mol. Cell Biol. *8*, 129–143.

van Antwerpen, R., Chen, G.C., Pullinger, C.R., Kane, J.P., LaBelle, M., Krauss, R.M., Luna-Chavez, C., Forte, T.M., and Gilkey, J.C. (1997). Cryo-electron microscopy of low density lipoprotein and reconstituted discoidal high density lipoprotein: imaging of the apolipoprotein moiety. J. Lipid Res. *38*, 659–669.

Vance, J.E. (1990). Phospholipid synthesis in a membrane fraction associated with mitochondria. J. Biol. Chem. *265*, 7248–7256.

Vance, J.E. (2020). Inter-organelle membrane contact sites: implications for lipid metabolism. Biol. Direct *15*, 24.

Walther, T.C., Chung, J., and Farese, R.V., Jr. (2017). Lipid Droplet Biogenesis. Annu. Rev. Cell Dev. Biol. *33*, 491–510.

Wang, X., and Schwarz, T.L. (2009). The mechanism of Ca2+ -dependent regulation of kinesin-mediated mitochondrial motility. Cell *136*, 163–174.

Wang, C.W., Miao, Y.H., and Chang, Y.S. (2014). A sterol-enriched vacuolar microdomain mediates stationary phase lipophagy in budding yeast. J. Cell Biol. *206*, 357–366.

Wang, P.T.C., Garcin, P.O., Fu, M., Masoudi, M., St-Pierre, P., Panté, N., and Nabi, I.R. (2015). Distinct mechanisms controlling rough and smooth endoplasmic reticulum contacts with mitochondria. J. Cell Sci. *128*, 2759–2765.

Wanker, E.E., Sun, Y., Savitz, A.J., and Meyer, D.I. (1995). Functional characterization of the 180-kD ribosome receptor in vivo. J. Cell Biol. *130*, 29–39.

Wehnekamp, F., Plucińska, G., Thong, R., Misgeld, T., and Lamb, D.C. (2019). Nanoresolution real-time 3D orbital tracking for studying mitochondrial trafficking in vertebrate axons in vivo. eLife *8*, 1–22.

Wei, E., Ben Ali, Y., Lyon, J., Wang, H., Nelson, R., Dolinsky, V.W., Dyck, J.R.B., Mitchell, G., Korbutt, G.S., and Lehner, R. (2010). Loss of TGH/Ces3 in mice decreases blood lipids, improves glucose tolerance, and increases energy expenditure. Cell Metab. *11*, 183–193.

Westermann, B. (2010). Mitochondrial fusion and fission in cell life and death. Nat. Rev. Mol. Cell Biol. *11*, 872–884.

Wetterau, J.R., Combs, K.A., Spinner, S.N., and Joiner, B.J. (1990). Protein disulfide isomerase is a component of the microsomal triglyceride transfer protein complex. J. Biol. Chem. *265*, 9800–9807.

Wong, Y.C., Ysselstein, D., and Krainc, D. (2018). Mitochondria-lysosome contacts regulate mitochondrial fission via RAB7 GTP hydrolysis. Nature *554*, 382–386.

Wyant, G.A., Abu-Remaileh, M., Frenkel, E.M., Laqtom, N.N., Dharamdasani, V., Lewis, C.A., Chan, S.H., Heinze, I., Ori, A., and Sabatini, D.M. (2018). Nufip1 is a ribosome receptor for starvation-induced ribophagy. Science *360*, 751–758.

Yan, Z., Yan, H., and Ou, H. (2012). Human thyroxine binding globulin (TBG) promoter directs efficient and sustaining transgene expression in liver-specific pattern. Gene *506*, 289–294.

Yu, Y., Kuang, Y.-L., Lei, D., Zhai, X., Zhang, M., Krauss, R.M., and Ren, G. (2016). Polyhedral 3D structure of human plasma very low density lipoproteins by individual particle cryo-electron tomography[1]. J. Lipid Res. *57*, 1879–1888.

Zhao, S., Jang, C., Liu, J., Uehara, K., Gilbert, M., Izzo, L., Zeng, X., Trefely, S., Fernandez, S., Carrer, A., et al. (2020). Dietary fructose feeds hepatic lipogenesis via microbiota-derived acetate. Nature *579*, 586–591.

Zhou, Y., Shaw, N., Li, Y., Zhao, Y., Zhang, R., and Liu, Z.-J. (2010). Structure-function analysis of human l-prostaglandin D synthase bound with fatty acid molecules. FASEB J. *24*, 4668–4677.

STAR★METHODS

KEY RESOURCES TABLE

REAGENT or RESOURCE	SOURCE	IDENTIFIER
Antibodies		
β-actin	Cell Signaling Technology	Cat#4970; RRID:AB_2223172
ADFP/Perilipin-2	Abcam	Cat#ab108323; RRID:AB_10863476
Albumin	Cell Signaling Technology	Cat#4929; RRID:AB_2225785
ApoB rabbit polyclonal	Abcam	Cat#ab20737 Lot#GR3176056-6; RRID:AB_2056954
ApoB goat polyclonal	EMD Millipore	Cat#AB742; RRID:AB_92217
ApoE rabbit polyclonal	Abcam	Cat#Ab20874; RRID:AB_449883
ApoE goat polyclonal	EMD Millipore	Cat#AB947; RRID:AB_2258475
ATP1a1	Cell Signaling Technology	Cat#3010; RRID:AB_2060983
BiP/Grp78	BD Biosciences	Cat#610978; RRID:AB_398291
Calnexin	StressMarq Biosciences	Cat#SPC-127; RRID:AB_2068995
Calreticulin	Cell Signaling Technology	Cat#12238; RRID:AB_2688013
Catalase	Thermo Fisher Scientific	Cat#702732; RRID:AB_2716888
Cathepsin C	Santa Cruz Biotechnology	Cat#sc-74590; RRID:AB_2086955
Ces1d	Wei et al., 2010	N/A
GFP	Cell Signaling Technology	Cat#2956; RRID:AB_1196615
GAPDH	Ambion	Cat#AM4300; RRID:AB_2536381
GM130/Golga2	BD Biosciences	Cat#610822; RRID:AB_398141
Mn SOD	Enzo Life Sciences	Cat#ADI-SOD-110-D; RRID:AB_2039585
Mttp	Atlas Antibodies	Cat#HPA054862 Lot#R72807; RRID:AB_2682628
MUP	Santa Cruz Biotechnology	Cat#sc-166429; RRID:AB_2017298
OPA1	BD Biosciences	Cat#612607; RRID:AB_399889
PMP70	Sigma-Aldrich	Cat#SAB4200181; RRID:AB_10639362
Rrbp1	Abcam	Cat#ab95983 Lot#GR47551; RRID:AB_10678752
S6 Ribosomal Protein	Cell Signaling Technology	Cat#2317; RRID:AB_2238583
phosphorylated-S6 (Ser204/244)	Cell Signaling Technology	Cat#5364; RRID:AB_10694233
Synj2bp	Sigma-Aldrich	Cat#HA000866; RRID:AB_2276678
anti-ApoE rabbit polyclonal	Abcam	Cat#ab52607 Lot#GR103096-3; RRID:AB_867704
anti-Rabbit IgG (H&L), gold-conjugated (10 nm)	Electron Microscopy Sciences	Cat#25109
anti-Rabbit IgG (H&L), gold-conjugated (15 nm)	Electron Microscopy Sciences	Cat#25113
anti-Mouse IgG	Jackson ImmunoResearch	Cat#115-035-062; RRID:AB_2338504
anti-Rabbit IgG	GE Healthcare	Cat#NA934; RRID:AB_772206
anti-Goat IgG	Thermo Fisher Scientific	Cat#81-1620; RRID:AB_2534006
anti-GFP antibody	Clontech Laboratories Inc.	Cat#632592; RRID: AB_2336883
Bacterial and virus strains		
AAV8-GFP-U6-mRrbp1-shScr	Vector Biolabs	Lot#181119/190107
AAV8-GFP-U6-mRrbp1-shRNA	Vector Biolabs	Lot#180917/191007
pENN.AAV.TBG.PI.ffLuciferase.RBG	Chang et al., 1999	Cat#105538-AAV8 Addgene
AAV.TBG.PI.Cre.rBG	Chang et al., 1999	Cat#107787-AAV8 Addgene
Chemicals, peptides, and recombinant proteins		
Poloxamer-407	Sigma-Aldrich	Cat#16758
Critical commercial assays		
Triglyceride colorimetric assay kit	Pointe Scientific Inc.	Cat#T7532-120
Cholesterol colorimetric assay kit	Pointe Scientific Inc.	Cat#C7510-120

(*Continued on next page*)

Continued

REAGENT or RESOURCE	SOURCE	IDENTIFIER
Deposited data		
WAM- and ER-enriched fractions proteomics	ProteomeXchange Consortium via PRIDE	PRIDE:PXD021826
Liver and WAM-enriched fractions transcriptomics	GEO Data Repository	GEO:GSE134777
WAM- and ER-enriched fractions lipidomics	This paper	Table S4 and S5
Experimental models: organisms/strains		
Adult male C57BL/6N mice (8 weeks of age)	Charles River	Stain code: 027
Mttp-floxed male mice	Chang et al., 1999	N/A
Oligonucleotides		
shScr sequence: 5′- CAACAAGATGAAGAGCACCAA-3′	Vector Biolabs	Lot#181119/190107
shRrbp1 sequence: 5′-CCGG-GCAGTCAGTTCTATTGTG AATCTCGAGATTCACAATAGAACTGACTGC-TTTTT-3′	Vector Biolabs	Lot#180917/191007
Software and algorithms		
ImageJ	N/A	https://imagej.nih.gov/ij/
Amira	Thermo Fisher Scientific	v. 2019.1
Prism	GraphPad	v.9
Excel	Microsoft	v. 16.25

RESOURCE AVAILABILITY

Lead contact

Further information and requests for resources and reagents should be directed to and will be fulfilled by the Lead Contact, Luca Pellegrini (luca.pellegrini@fmed.ulaval.ca).

Materials availability

All Adeno-associated virus vectors generated in this study are available upon request from Vector Biolabs.

Data and code availability

All data are available in the manuscript or in the supplementary materials.

The accession number for the mass spectrometry proteomics data reported in this paper is PRIDE: PXD021826.

The accession number for the RNA sequencing data reported in this paper is GEO: GSE134777.

EXPERIMENTAL MODEL AND SUBJECT DETAILS

Adult male C57BL/6N mice (8 weeks old) were purchased from Charles River; *Mttp*-floxed mice were a generous gift from Dr. Mahmood M. Hussain and Dr. Chan Lawrence (Chang et al., 1999). The mice were housed in a pathogen-free animal facility under a 12 h light/dark cycle at constant temperature and humidity and fed standard rodent chow and water *ad libitum*. All experiments were conducted with male mice 9-12 weeks old. For fasting/refeeding studies, animals were either fasted for 14 hours overnight with water *ad libitum* and sacrificed in the morning or fasted for 12 hours overnight with water *ad libitum* and, in the morning, they were provided standard rodent chow and sugary water (30% sucrose) *ad libitum* for three hours. Livers were removed immediately after anesthetization of the animals with 2% isoflurane and sacrificed through cervical dislocation. For liver and small intestine samples cryo-fixation, animals were anesthetized by intraperitoneal injection with ketamine; 3-5 tissue biopsies were collected using the Rapid Transfer System (Leica) and vitrified by high-pressure-freezing (Leica EM PACT2). Mice were then sacrificed by cervical dislocation. All experiments involving animals were approved by the animal protection committee of Laval University (CPAUL) and performed in accordance with its guidelines for animal welfare.

METHOD DETAILS

Energy balance model of the wrappER-mitochondria contact

Theoretical and experimental approaches rooted in physics have been developed to describe many aspects of the conformational behavior of interacting membranes (Knorr et al., 2012; Lipowsky, 1991) and to address the morphology of cellular organelles such as the Golgi complex (Campelo et al., 2017). The paradigm emerging from these studies is that the free energy of a membrane reaches a

minimum when the membrane is flat or closed in a vesicle-like structure (Campelo et al., 2017; Knorr et al., 2012; Lipowsky, 1991; Steinkühler et al., 2020).

The wrappER can assume concave and convex curvatures of considerable magnitude (Videos S1, S2, and S3) that are maintained during fasting-to-feeding transitions (Figure 1H). This suggests that the contact between the wrappER and mitochondria is not a random consequence of the two organelles ''parking'' against each other but instead the product of dedicated mechanisms that bend the rough-ER around the mitochondrion and preserve the energy associated with its curvature (i.e., tethers). In physical terms, this implies demonstrating that the free energy of the wrappER membrane with a radius of curvature similar to that of the mitochondrion is always greater than the free energy the wrappER would have if it were flat or closed as a spherical vesicle. In other words, if wrapping around mitochondria is thermodynamically unfavorable, dedicated mechanisms must exist to maintain the wrappER association with mitochondria.

To model the free energy change associated with the wrappER-mitochondria contact, reasonable simplifying assumptions have to be made. For example, we consider the shape of the mitochondria to be spherical rather than irregular (Figure S9A).

Our model assumes that:

1) The mitochondrion is a passive, rigid, spherical organelle of radius R and mean curvature $M = 1/R$ that does not contribute to the total energy of the curvature of the wrappER membrane.
2) The wrappER is a spherical membrane cupped above the mitochondrion (Figure S9A, lower panel). Its surface S is composed of the cytosolic face S_1, with the area A_1 and mean curvature M_1, and the mitochondrial face S_2, with the area A_2 and mean curvature M_2 (Figure S9B). A_1 and A_2 are similar and constitute the area A of the wrappER where $A_1 = A_2 \approx A$. S_1 and S_2 are connected by a region that forms the edge of the wrappER where the membrane bends on itself at 180 degrees, with a small radius r_{min} and surface S_3 (Figure S9B). The value of the mean curvature of the edge (Knorr et al., 2012) of the wrappER ($M_3 = \mathbf{1}/\mathbf{2}r_{min}$) is similar to that of a flat rough-ER sheet and, therefore, is negligible in determining M_1 and M_2 (Figure S9C).
3) The spontaneous curvature (Seifert, 1997) of the wrappER C_S (imposed by its phospholipid and protein composition (McMahon and Gallop, 2005; Di Paolo and De Camilli, 2006) is set to a constant value in all its parts (Campelo et al., 2017; Knorr et al., 2012): $C_S = C_1 = C_2 = C_3$ (see also *Note I*).
4) The distance between S_1 and S_2, as well as the distance between S_2 and the mitochondrial surface, are small compared to R. Therefore, the mean curvatures M_1 and M_2 can be approximated by $M_1 = -M_2 = 1/R_{wER}$, where R_{wER} is the radius of curvature of the wrappER.
5) The wrappER is composed of a phospholipid membrane that can be described by continuum mechanics, with a bending rigidity equivalent to that of the rough-ER (Helfrich, 1973; Seifert, 1997).
6) Gravitational, electromagnetic, van der Waals, electrostatic, and solvation attractive and repulsive forces (Israelachvili, 2011) do not contribute to maintain either the curvature of the wrappER or the distance separating it from the mitochondrial surface.
7) Microtubule-dependent mechanisms of intracellular mitochondrial transport/movement (Sheng and Cai, 2012) that could ''push'' a mitochondrion against a rough-ER membrane are not involved in maintaining the curvature of the wrappER and its distance from the surface of the mitochondrion.

Given this set of assumptions, the curvature energy E of a round patch of rough-ER wrapped around the mitochondrion (Helfrich energy; Helfrich, 1973; Hu et al., 2012; Knorr et al., 2012; Lipowsky, 1991; Seifert, 1997) can be written as:

$$E = 2\kappa \int_S (M - Cs)^2 dA \tag{1}$$

where κ is a constant that represents the bending rigidity of the wrappER (see also *Note II*).

Accordingly, the energy required to bend the rough-ER/wrappER to a curvature $1/R_{wER}$ is described by the following equation:

$$\frac{1}{4\pi\kappa} E(\eta) = 4\eta^2 + r_{rim}\left[\frac{1}{2r_{rim}} - C_3\right]^2 \sqrt{\pi A}\sqrt{1-\eta^2} + AC_S^2 \Big/ \pi \tag{2}$$

where $\eta = \sqrt{A/4\pi R_{wER}^2}$ is the dimensionless mean curvature of the wrappER. We need only to consider values of η that range from 0, when the wrappER is flat (Figure S9D, top panel), to 1, when the wrappER assumes a closed vesicle-like conformation (Knorr et al., 2012) (Figure S9D, lower panel) (see also Note III). The first derivative of Equation 2 is given by:

$$\frac{1}{4\pi\kappa}\frac{dE}{d\eta} = \eta\left(8\eta - r_{rim}\left[\frac{1}{2r_{rim}} - C_3\right]^2 \sqrt{\pi A}\ \frac{1}{\sqrt{1-\eta^2}}\right)$$

Notice that, near $\eta \approx 1$, the slope is always negative, implying a decreasing energy function. Near $\eta \approx 0$, there are two possible values of the slope. If the parameter values are chosen such that the slope is initially negative for $\eta \approx 0$, then, the energy always decreases, and the minimum free energy occurs for $\eta = 1$. If the slope is initially positive for $\eta \approx 0$, then, there is at most one possible maximum of free energy for $0 < \eta < 1$, whereas the minimum free energy would occur at either $\eta = 0$ or $\eta = 1$.

Equation 2 indicates that, regardless of the value of the intrinsic curvature of the edge C_3, the minimum free energy state is reached when the wrappER is either shaped as a spherical vesicle of area $A = 4\pi R_{wER}^2$, with energy $E = 16\pi\kappa + 4A\kappa C_S^2$, or is flat ($R_{wER} \rightarrow \infty$), with energy

$$\frac{1}{4\pi\kappa}\mathrm{E} = r_{rim}\left[\frac{1}{2r_{rim}} - C_3\right]^2\sqrt{\pi A} + AC_S^2\Big/\pi$$

We conclude, therefore, that the wrappER-mitochondria contact described in this work cannot be the product of a random "parking" of the two organelles against each other. This is the case because, according to our model, wrapping around the mitochondria is thermodynamically unfavorable; therefore, that persistent curvature of the wrappER around the mitochondrion (i.e., $R \approx R_{wER}$) has to be maintained through the constant expenditure of chemical energy, which appears highly unlikely, or has to be conserved through the recruitment of tethering-like proteins. Indeed, without either these mechanisms in action, the wrappER would flatten in a "standard" rough-ER-like planar geometry or assume a vesicle-like structure (Carter et al., 2020).

Note I The case where C_1 is substantially different from C_2 could predict the existence of a state with a minimum energy in which the shape of the wrappER is neither flat nor spherical. For this to be the case, it is required that $R_{wER} \neq R$, a condition that is inconsistent with the observation that R_{wER} is approximately equal to the mean curvature radius of the mitochondrion. Therefore, the only possibility is that $\boldsymbol{R \approx R_{wER}}$.

Note II This equation does not include the Gaussian curvature energy because, according to our assumptions, it is a constant independent of the wrappER geometry and, therefore, can be disregarded for our purposes (Knorr et al., 2012).

Note III We need only consider positive values of η since a wrapper with a negative η would bend away from the mitochondrion, contrary to our observations, and support the need for additional forces to maintain the persistent curvature of the wrappER.

Blood plasma collection and *in vivo* VLDL secretion analysis

Mice were fasted for 6 h and injected intraperitoneally with the lipase inhibitor Poloxamer-407 (P-407; 1 g kg^{-1}; Sigma-Aldrich); blood was collected just before and at 1, 2 and 3 h after P-407 injection. For each sample, 60 μL of blood was collected from the caudal vein in heparinized capillary tubes and immediately centrifuged at 2,100 g for 12 min to prepare plasma fractions. Plasma was flash-frozen in dry ice and stored at −30°C until needed. Plasma TAG and total cholesterol measurements were performed using commercial colorimetric assays kits according to manufacturer's instructions (Pointe Scientific Inc.).

Immunoblot analysis

Total protein concentration was determined using high-precision, detergent-compatible assay (BCA Protein Assay Reagent; Thermo Fisher Scientific). Protein samples were analyzed by SDS-PAGE using the following types of precast gels according to manufacturer's instructions: NuPAGE 3%–8% Tris-Acetate Protein gels, Bolt 8% Bis-Tris Plus gels, Bolt 12% Bis-Tris Plus gels, Bolt 4%–12% Bis-Tris Plus gels (Thermo Fisher Scientific). Western blotting was performed by transferring proteins for 60 min at 100V to a PVDF membrane (Immobilon, Millipore; 0.45 μm pore size) in transfer buffer (20% methanol; 320 mM glycine, 20 mM Tris-base pH 8.4). For blots that were analyzed with anti-Rrbp1 and anti-ApoB antibodies, proteins were transferred for 80 min or 90 min at 100V, respectively (Immobilon, Millipore). Membranes were blocked for 60 min at room temperature with 7.5% nonfat milk in Tris-buffered saline, 0.1% Tween-20. Primary antibodies were incubated overnight at 4 °C in 5% nonfat milk or 5% bovine serum albumin (BSA; Thermo Fisher Scientific). The primary antibodies used in this study were the following: β-actin (Cell Signaling Technology #4970; 1:6,000-1:10,000), ADFP/Perilipin-2 (Abcam #ab108323; 1:1000), Albumin (Cell Signaling Technology #4929; 1:10,000), ApoB (rabbit polyclonal Abcam #ab20737 (Syed et al., 2017), 1:2,000; goat polyclonal EMD Millipore #AB742, 1:5,000), ApoE (Abcam #Ab20874 (Arnold et al., 2015; Becker et al., 2010), 1:1,000; goat polyclonal EMD Millipore #AB947 1:1,000), ATP1a1 (Cell Signaling Technology #3010; 1:750), BiP/Grp78 (BD Biosciences #610978; 1:50,000), Calnexin (StressMarq Biosciences #SPC-127; 1:20,000-30,000), Calreticulin (Cell Signaling Technology #12238; 1:75,000-1:150,000), Catalase (Thermo Fisher Scientific #702732; 1:100,000), Cathepsin C (Santa Cruz Biotechnology #sc-74590; 1:1,000), Ces1d (1:80,000) (Wei et al., 2010), GFP (Cell Signaling Technology #2956; 1:1,000), GAPDH (Ambion #AM4300; 1:400,000), GM130/Golga2 (BD Biosciences #610822; 1:750), Mn SOD (Enzo Life Sciences #ADI-SOD-110-D; 1:8,000), Mttp (Atlas Antibodies #HPA054862; 1:1,000-2,000), MUP (Santa Cruz Biotechnology #sc-166429; 1:60,000), OPA1 (BD Biosciences 612607; 1:11,000) (Sood et al., 2014), PMP70 (Sigma-Aldrich #SAB4200181; 1:18,000), Rrbp1 (Abcam #ab95983; 1:2,000) (Hung et al., 2017), S6 Ribosomal Protein (Cell Signaling Technology #2317; 1:750), phosphorylated-S6 (Ser204/244) (Cell Signaling Technology #5364; 1:3,000) (Sood et al., 2014), Synj2bp (Sigma-Aldrich #HA000866; 1:750). The HRP-conjugated secondary antibodies used in this study were the following: anti-Mouse IgG (Jackson ImmunoResearch #115-035-062; 1:5,000-10,000), anti-rabbit IgG (GE Healthcare #NA934; 1:5,000-10,000), and anti-goat IgG, HRP (Thermo Fisher Scientific #81-1620; 1:5,000). Protein bands were detected by chemiluminescence using the SuperSignal ELISA Femto substrate (Thermo Fisher Scientific) and the VersaDoc 3000 CCD imaging system (Bio-Rad Laboratories). The specificity of the anti-MUP antibody in immunoblot analysis was assessed using a recombinant MUP1 protein (ImmunoDiagnostics Limited #42150). The specificity of the anti-Mttp antibody in immunoblot analysis was validated by preabsorbing it with 10-fold excess of the recombinant protein (Atlas Antibodies #APrEST85548, lot #PRL02977), and by the knock-out experiments shown in Figure 7F.

See Data S2 for the original, uncropped immunoblots.

Preparation of cellular fractions enriched in wrappER-associated mitochondria from the mouse liver

Mouse liver was quickly excided, rinsed three times with Elution Buffer (EB; 10 mM Tris-HCl, 1 mM $MgCl_2$, 0.1 mM EGTA, pH 7.4) supplemented with 250 mM Sucrose (EB10), chopped in small pieces and resuspended in 5 mL EB10 supplemented with Protease Inhibitor Cocktail (PIC; Thermo Fisher Scientific, #78429). The sample was mechanically homogenized with 16 strokes in a glass-teflon dounce homogenizer, brought to 12 mL volume with EB10 supplemented with PIC and poured in two 30 mL glass centrifuge tubes. The homogenate was spun for three times at 400 g for 10 min at 4°C and, at the end of the centrifugation, the supernatants were collected and mix together to obtain the mouse liver whole lysate (WL). 7 mL of WL were carefully layered on top of 7 mL of a 27% w/w sucrose solution (27% sucrose in EB) inside a 50 mL Falcon tube and spun at 2000 g for 20 min at 4°C; the pellet thus obtained represents the WAM-enriched fraction. At the end of the centrifugation, the top 5 mL of the supernatant were divided in 2 mL Eppendorf tubes, spun twice at 12000 g for 10 min at 4°C, and the pellets discarded. 1.5 mL of the resulting supernatant were mixed in a 50 mL Falcon tube with 22.5 mL of ice cold $CaCl_2$ 8 mM solution, incubated for 15 min at 4°C with gentle rocking, transferred into two 30 mL glass tubes and centrifugated at 8,000 g for 10 min at 4°C. The resulting pellets represent the ER-enriched fraction.

WAM-enriched fraction fixation and embedding for electron microscopy

WAM-enriched fractions were gently resuspended in 27% w/w sucrose solution (27% sucrose in EB), pelleted at 3000 g for 10 min at 4°C and incubated overnight in 500 μL of 27% w/w sucrose solution containing 2% glutaraldehyde, at 4°C. The pellet was rinsed three times with 27% w/w sucrose solution and incubated in 1% (w/v) osmium tetroxide in ddH_2O for 40 min at room temperature, in the dark. After 3 washes with EB10, pellet was dehydrated in ethanol 50%, 70% (supplemented with 1% Uranyl Acetate, for 1h in the dark) 90%, 100%, followed by two incubation in 100% propylene oxide for 20 min at RT and embedded in Epoxy resin.

Tissue sample preparation for EM analysis, ET imaging and 3D reconstruction

Mouse liver and small intestines were quickly biopsied using Rapid Transfer System (Leica). High-pressure freezing (Leica EM PACT2) was used for cryo-fixation of the samples. Freeze substitution was performed with the Leica automatic freeze substitution (AFS) chamber. The substitution fluid was acetone containing 1% OsO_4 and 0.1% uranyl acetate. The procedure started at –90°C for 8 h and warmed up to –60°C at the speed of 5°C/h. Substitution medium was replaced with pure acetone after the temperature reached 0°C. Samples were embedded in Araldite/Epon/Dodecenylsuccinic anhydride (DDSA) and 2,4,6-tris (dimethylaminomethyl) phenol (DMP30) mixture [araldite/epon stock, epoxy 41% (wt/wt), durcupan Araldite casting resin M (ACM) 54% (wt/wt), dibutylphthalate 5% (wt/wt); araldite/epon complete formulation, araldite/epon stock 49% (wt/wt), hardener DDSA 49% (wt/wt), and accelerator DMP-30 2% (wt/wt)]. Procedure was performed stepwise: 33% resin in water-free acetone for 4 h, 66% resin in water-free acetone for hours, 100% resin overnight, and one 100% resin change before polymerization. All samples were polymerized at 58°C for at least 48 h. Samples were cut at 50 nm and put on single-slot copper grids using a Leica Ultramicrotome. After counterstaining with lead citrate, samples were viewed on a Tecnai-12 by Philips with a Megaview camera using the Analysis software.

For serial section electron tomography (SSET), serial thick sections were collected on formvar-coated copper slot grids and gold fiducials (10nm) were applied on both surfaces of the grids. The samples were imaged in a 200 kV Tecnai G2 20 electron microscope (FEI) or a 120kV Talos L120C (Thermo Fisher Scientific). Tilted images (+65/-65 according to a Saxton scheme) were acquired using Xplorer 3D (FEI) with an Eagle 2k × 2k CCD camera (FEI) or TEM Tomography 4.0 acquisition software using a 4kx4k Ceta16M camera (Thermo Fisher Scientific). Tilted series alignment and tomography reconstruction was done with the IMOD software package (Mastronarde, 1997).

3D reconstruction analysis

For each ET analysis, serial tomograms were compiled as a single TIFF file and analyzed in Amira Software (v. 2019.1; Thermo Fisher Scientific). The z scale was stretched using a 1.6 factor to correct for resin shrinkage. The structure of interest (e.g., mitochondrion, wrappER, ribosome, etc.) was carefully manually traced on each virtual slice using a graphic tablet and then reconstructed in 3D, with rendering generated using unconstrained smoothing parameters (for smaller structures like ribosomes, existing weights parameters were used). Movies were generated in Amira Software and then edited with iMovie (v. 10.1.10; Apple).

2D-EM morphometric analysis

All the morphometric studies showed in the manuscript were conducted on high quality TEM images using a graphic tablet (with the exception of the measurements of Figure S1D, which were performed on ET images). Mitochondria-wrappER distance, coverage, cleft area, adhesion site and MAM analysis were measured using ImageJ (NIH). In the 3D reconstruction analysis, MAM, wrappER and mitochondrial surface areas were measured using Amira Software. Data were analyzed and plotted using Excel (v.16.25; Microsoft) and Prism (v.9; GraphPad).

Lipoproteins imaging by negative staining and immunogold EM analysis

Animals were fasted for 12 hours overnight with water *ad libitum*; in the morning they were provided standard rodent chow and sugary water (30% sucrose) *ad libitum* for three hours. Livers were explanted and WAM-enriched fractions freshly prepared as described in "Preparation of Cellular Fractions Enriched in WrappER-Associated Mitochondria from The Mouse Liver"; however, for lipoproteins analysis the last step consisted in resuspending the WAM-containing pellet in 600 μL of TBS (150 mM NaCl, 10 mM Tris-HCl pH 7.6) supplemented with 1x Halt protease inhibitor cocktail (Thermo Fisher Scientific). Membranes (containing approx. 1 mg of proteins)

were permeabilized by adding 600 μL of TBS 0.1% Triton X-100, followed by incubation at 4 °C for 30 min and deep freeze-and-thaw. The permeabilized WAM-enriched fraction was transferred to a 4 mL ultracentrifuge tube containing 1.8 mL of 0.5 x TBS and centrifuged for 1 hr at 400,000 g in a SW60-Ti rotor (Beckman Coulter). Floated lipoproteins were recovered by skimming the top 100 μL of the supernatant and placed (2.5 μl) on glow-discharged carbon-coated 300 mesh copper grids (SPI Supplies). After 5 min of incubation at RT, the grids were blocked for 10 min with 50 μL of PBSB (PBS, 0.5% BSA-c; Electron Microscopy Sciences), followed by incubation with anti-ApoE rabbit polyclonal antibody diluted 1:50 in PBSB for 30 min at RT (Abcam #ab52607, lot #GR103096-3) (Syed et al., 2017). Grids were then washed 3 times at RT with PBSB (2 min per wash) and incubated at RT for 30 min with gold-conjugated (10 nm) secondary antibody (diluted 1:100 in PBSB; Goat-anti-Rabbit IgG (H&L), Electron Microscopy Sciences #25109). Grids were washed 3 times at RT with PBSB (2 min per wash) and incubated at RT for 30 min with normal rabbit serum to saturate with IgG open binding sites on the secondary antibody (diluted 1:10 in PBSB; Electron Microscopy Sciences #25568). Following a single wash in PBSB, grids were incubated with Fab fragments (diluted 1:20 in PBSB; Jackson ImmunoResearch #111-007-003) to cover the rabbit IgG so that the second secondary antibody would not bind to it. Grids were then washed 3 times at RT with PBSB (2 min per wash) and incubated for 30 min at RT with anti-ApoB rabbit polyclonal antibody (diluted 1:50 in PBSB; Abcam #ab20737 (Syed et al., 2017), lot #GR3176056-6). Finally, grids were washed and incubated at RT for 30 min with gold-conjugated (15 nm) secondary antibody (diluted 1:100 in PBSB; Goat-anti-Rabbit IgG (H&L), Electron Microscopy Sciences #25113). After three washes in PBSB the grids were stained with 1% uranyl formate according to well-established EM protocols optimized for lipoproteins studies (Garewal et al., 2013). Lipoproteins were imaged by TEM with a Tecnai-12 microscope (Philips).

Pre-embedding immunogold EM analysis on WAM-enriched fractions

Anti-Rrbp1 and Anti-ApoB immunogold analysis

Mouse liver WAM-enriched fractions were prepared as described in "preparation of cellular fractions enriched in wrappER-associated mitochondria from the mouse liver." The WAM-containing pellet was gently resuspended with a small, soft paintbrush in 150 μL of EB27 (10 mM Tris-HCl, 1 mM $MgCl_2$, 0.1 mM EGTA, sucrose 27% w/w, pH 7.4, supplemented with PIC - Thermo Fisher Scientific); 50 μL of this slurry was transferred to an Eppendorf tube containing 150 μL of EB27 and 3 μL of anti-Rrbp1 or anti-ApoB rabbit polyclonal antibody (Abcam #ab95983, lot #GR47551; Abcam #ab20737 (Syed et al., 2017), lot #GR3176056), and the mix was incubated for 4 hours at 4 °C with gentle rocking. Following primary antibody incubation, 150 μL of EB-27 containing 3 μL of gold-conjugated (10 nm) secondary antibody was added (Goat-anti-Rabbit IgG H&L; Electron Microscopy Sciences #25109) and the mix was incubated 1 hr at RT with gentle rocking. The slurry was centrifuged for 10 min at 5,000 g at 4 °C. The pellet was gently resuspended and washed twice with 500 μL of EB27. Finally, the pellet was fixed by incubation overnight at 4 °C with 500 μL of EB27/paraformaldehyde 16% (3:1 v/v). Pellet embedding was performed as described in "WAM-enriched fraction fixation and embedding for electron microscopy."

Anti-Mttp immunogold analysis

WAM-enriched mouse liver fractions were prepared as described in "Preparation of Cellular Fractions Enriched in WrappER-Associated Mitochondria from The Mouse Liver." The WAM-containing pellet was fixed by incubation overnight at 4 °C with 500 μL of EB27/paraformaldehyde 16% (3:1 v/v) and then gently immersed in a solution composed by 4% low melting agarose gel (Agarose II; Amresco #0815) dissolved in EB10 (10 mM Tris-HCl, 1 mM $MgCl_2$, 0.1 mM EGTA, 250mM sucrose, pH 7.4) at 30-35 °C. Upon gel solidification at 4°C for 1 hour, the sample was cut with an automated vibratome (Leica VT1200S) in slices of 50 μm of thickness. Slices were washed from the paraformaldehyde three times in TBS and then incubated for 30 min at 4 °C in blocking solution 1 (2% BSA, 5% nonfat milk, 5% normal rabbit serum, 0.1 g/ml glycine, 0.5 g/ml L-lysine, 0.01% Triton X-100 in TBS) followed by overnight incubation at 4 °C with anti-Mttp rabbit polyclonal antibody (1:100; Atlas Antibodies #HPA054862, lot #R72807) diluted in TBS and blocking solution 1 (9:1 v/v). Slices were washed three times in TBS and incubated for 30 min in blocking solution 2 (0.8% BSA, 0.1% CWFS-gelatin, 2% normal rabbit serum, 0.1 g/ml glycine, 0.1 g/ml L-lysine in TBS). The gold-conjugated secondary antibody (F(ab')2 Fragment of Goat-anti-Rabbit IgG (H&L); Electron Microscopy Sciences #25360) was diluted 1:100 in blocking buffer 2, incubated overnight at 4 °C and then washed three times in TBS. Mttp-antibodies complexes were crosslinked by incubating the agarose slices in TBS 1% glutaraldehyde for 10 min. Slices were then first washed three times with phosphate buffer (19 mM NaH_2PO_4, 81 mM Na_2HPO_4, pH 7.4) and then once with deionized water before silver enhancement reagents were applied according to manufacturer's instructions (12 min incubation, GE Healthcare Lifescience #RPN491). After three washes in deionized water and phosphate buffer, slices were processed for embedding in Epoxy resin according to standard EM protocols and procedures (described in WAM-enriched fraction fixation and embedding for electron microscopy).

Immunogold quantification of labeling distribution and specificity

The specificity and preferential localization of the immunogold staining was performed as described (Mayhew et al., 2002). Specifically, we utilized the Model II (membrane surface compartments) explained in this study and used ImageJ with the Plugin Grid using the following settings: grid type: horizontal lines; area per point: 3 $pixels^2$; center grid on image. The number of EM images analyzed per immunogold assay are indicated in column 2 of Figures S5A, S5B, and S6D.

Immunohistochemistry

Livers were explanted three weeks after injection with $1.8x10^{11}$ gc/mouse of AAV8-GFP-shRNA, fixed overnight in PFA 4%, and sectioned with an automated vibratome (Leica VT1200S). Tissue sections were incubated in PBS 3% H_2O_2 for 25 min at RT,

permeabilized with PBS 0.2% Triton X-100 containing 4% non-fat milk for 2 hr at RT and incubated overnight at 4°C with Living Colors rabbit polyclonal anti-GFP antibody (Clontech Laboratories, Inc. #632592; 1:500). Sections were extensively washed and incubated for 2 hr at RT with HRP-conjugated anti-rabbit IgG (GE Healthcare #NA934; 1:500). Following additional extensive washing, GFP immunolabeling was revealed incubating for 10 min the liver sections in a solution containing 0.5% 3,3′-diaminobenzidine (DAB; Sigma-Aldrich #D8001), 0.04% H_2O_2 in Tris-HCl 0.05M (pH 7.5). Nuclear counterstaining was performed according to standard protocols using Gill II hematoxylin (Sigma-Aldrich #GHS216). Sections were dehydrated, mounted with DPX Mountant for histology (Sigma-Aldrich #06522), and imaged using an upright microscope (Leica Leitz DMRB) equipped with CCTV camera.

RNA isolation and sequencing

RNA sequencing analysis was conducted using the same six WAM fractions samples used for the proteomic analysis, and the liver transcriptome analysis was done on the mouse liver lysates from where the WAM fractions were prepared. Messenger RNA was isolated from mouse liver homogenates using the Dynabeads mRNA Direct Micropurification Kit (Thermo Fisher Scientific); of this, 250 ng were then used to prepare sequencing libraries using the NEBNext Ultra II directional RNA library prep kit for Illumina. The entire procedure was done according to manufacturer's instruction, and the libraries were prepared using nine amplification cycles. The quality of final amplified libraries was examined with a DNA screentape D1000 on a TapeStation 2200 and the quantification was done on the QBit 3.0 fluorometer (Thermo Fisher Scientific). The average insert size for the paired-end libraries was 260 bp. mRNA-seq libraries with unique index were pooled together in equimolar ratio and sequenced for paired-end 125 bp sequencing using one lane of a high output flow cell on an HiSeq 2500 V4 system (Illumina). To ensure the quality of the reads, we examined a variety of quality control metrics on raw and trimmed data to detect poorly performing samples, using a combination of FastQC (v. 0.11.5, Babraham Bioinformatics) and MultiQC (v. 1.5) (Ewels et al., 2016). Reads were trimmed using fastp (v. 0.12.4) (Chen et al., 2018) with the following options: length required 30, qualified quality phred 20, correction, cut by quality 3, cut window size 10 and cut mean quality 30. All other options used the default values. The quantification was performed with Kallisto (v. 0.44.0) (Bray et al., 2016) using the *Mus musculus* Ensembl release 92 transcriptome, filtered to keep only the standard chromosomes. Post-processing was performed in R (v. 3.5.0). Counts were normalized with the RUVseq package (v. 1.14.0) using mitochondrial genes as control genes. The transcriptomic analysis shown in this study was performed by the Genomics Center of the CHU de Québec-Université Laval Research Center, Québec City, Canada.

Protein mass spectrometry analysis

After acetone precipitation, protein pellets were resuspended in Buffer-1 (50 mM ammonium bicarbonate, 1% sodium deoxycholate, pH 8), and quantified using the Micro-Bredford assay (Bio-Rad). 10 μg of proteins was reduced at 37°C with DTT, alkylated with iodoacetamide, and digested overnight with trypsin. Proteolysis was stopped by acidification (3% acetonitrile, 1% TFA, 0.5% acetic acid) and peptides were purified on stage tip (C18), vacuum dried, and resuspended in 50 μL 0.1% formic acid. One tenth of this volume (1 μg) was separated by online reversed-phase nanoscale capillary liquid chromatography and analyzed by electrospray mass spectrometry (LC MS/MS) using an Ekspert NanoLC425 (Eksigent Technologies) coupled to a 5600+ mass spectrometer (Sciex) equipped with a nanoelectrospray ion source.

Tryptic peptides were trapped at 4 ml/min on a PepMap Acclaim C18 column (5 × 0.3 mm; Thermo FisherScientific) and eluted through a self-packed PicoFrit column (New Objective) filled with ReproSil C18 (3 μm, 180 × 0.075 mm, 120 Å; Dr Maisch GmbH). Separation was achieved with a 5%–35% acetonitrile gradient in 0.1% formic acid over 90 min at 300 nl/min.

Peptides were ionized by electrospray with 2.3 kV. Mass spectra were acquired using a data-dependent acquisition mode using Proteome Analyst software (v. 1.7) (Lu et al., 2004). Each full scan mass spectrum (400 to 1250 m/z) was followed by collision-induced dissociation of the twenty most intense ions. Dynamic exclusion was set for a period of 12 s and a tolerance of 100 ppm.

Database searching

Mascot generic format (MGF) peak list files were created using the Protein Pilot software (v. 4.5; Sciex). MGF sample files were then analyzed using Mascot (v. 2.5.1; Matrix Science). Mascot was setup to search the contaminants_thegpm_20170713.fasta and the REF_MusMusculus_ci_10090_up000000589_20180509 database (61364 entries) assuming the digestion enzyme trypsin. Mascot was searched with a fragment ion mass tolerance of 0.100 Da and a parent ion tolerance of 0.100 Da. Carbamidomethyl of cysteine was specified in Mascot as a fixed modification. Deamidation of asparagine and glutamine, as well as methionine oxidation, were specified in Mascot as variable modifications.

Criteria for protein identification

Scaffold (v. 4.8.6; Proteome Software Inc.) was used to validate MS/MS based peptide and protein identifications. Peptide identifications were accepted if they could be established at greater than 96.0% probability to achieve an FDR (False Discovery Rate) less than 1.0% by the Scaffold Local FDR algorithm. Protein identifications were accepted if they could be established at greater than 97.0% probability to achieve an FDR less than 1.0% and contained at least 1 identified peptide. Protein probabilities were assigned by the Protein Prophet algorithm (Nesvizhskii et al., 2003). Proteins that contained similar peptides and could not be differentiated based on MS/MS analysis alone were grouped to satisfy the principles of parsimony.

Protein digestion, mass spectrometry analyses and protein identification were performed by the Proteomics Platform of the CHU de Québec-Université Laval Research Center, Québec City, Canada.

Lipidomic analysis

Lipidomic analysis was done on either 100 mg of flash-frozen liver tissue or 0.25 mg/protein WAM- and ER-enriched fractions prepared as described in "Preparation of Cellular Fractions Enriched in WrappER-Associated Mitochondria from The Mouse Liver." Liver tissue samples were placed in a 2 mL homogenizer tube pre-loaded with 2.8 mm ceramic beads (Omni #19-628). PBS was added to the tube and the sample homogenized in the Omni Bead Ruptor Elite (3 cycles of 10 s at 5 m/s with a 10 s dwell time). For lipid extraction, 3-6 mg of liver homogenate or the entire WAM- and ER-enriched fractions were transferred to a glass tube and processed using the modified Bligh and Dyer extraction method (Bligh and Dyer, 1959). Prior to biphasic extraction, a 13-lipid class Lipidyzer Internal Standard Mix was added to each sample (Sciex #5040156). Following two successive extractions, pooled organic layers were dried using a Genevac EZ-2 Elite. Lipid samples were resuspended in 1:1 methanol/dichloromethane with 10 mM ammonium acetate and transferred to glass robovials for analysis (Thermo Fisher #10800107). Samples were analyzed on the Sciex Lipidyzer Platform for targeted quantitative measurement of 1100 lipid species across 13 classes. Differential Mobility Device on Lipidyzer was tuned with SelexION tuning kit (Sciex #5040141). Instrument settings, tuning settings, and MRM list are available upon request. The values were normalized by mg of sample used. Data analysis was performed on the Lipidyzer software at the UCLA lipidomics laboratory.

MAM activity assay

WAM-enriched fractions were isolated from livers of overnight fasted adult male C57BL/6N mice (n = 3). The MAM phospholipid synthesis/transfer/conversion was performed as described by Shiao et al. (1998) in technical triplicates. 100 μg WAM proteins in assay buffer (25 mM HEPES, 1 mM $CaCl_2$, 2 mM $MgCl_2$, pH = 7.4) were incubated with 10 μCi radiolabeled [^{3}H]-serine and 0.4 mM cold serine in a total volume of 200 μL. Samples were incubated for 3 h at 37°C. The reaction was stopped by addition of 4 mL chloroform/methanol (2:1) and 1.5 mL double distilled water. Lipids were extracted and separated by thin-layer chromatography. Lipids were visualized by exposure to iodine vapors. The radioactivity in phosphatidylserine and phosphatidylethanolamine was determined using a scintillation counter. Results were expressed as DPM/mg WAM protein.

AAV8-Shrna design and *in vivo* delivery

An adeno-associated virus serotype 8 (AAV8) encoding a short hairpin RNA (shRNA) construct targeting mouse *Rrbp1* (Genebank RefSeq NM_024281; targeting sequence: GCAGTCAGTTCTATTGTGAAT; shRNA sequence: 5′-CCGG-GCAGTCAGTTCTATTGT GAATCTCGAGATTCACAATAGAACTGACTGC-TTTTT-3′) driven by the U6 promoter was purchased from Vector Biolabs; this vector, AAV8-GFP-U6-mRrbp1-shRNA, also expressed eGFP driven by the CMV promoter and yielded ~90% knockdown of Rrbp1 expression in Hepa1.6 cells (Vector Biolabs). The control vector AAV8-GFP-U6-scrmb-shRNA encoded a short hairpin with a scrambled sequence (5′- CAACAAGATGAAGAGCACCAA-3′; Vector Biolabs). AAV8 particles were purified by two rounds of CsCl gradient purification, desalted and titered (titer: $> 2 \times 10^{13}$ GC/ml). AAV8 particles were diluted in sterile PBS and wild-type C57BL/6N mice (9–12 weeks old) were injected with either control vector (AAV8-shScr) or AAV8-GFP-U6-mRrbp1-shRNA (AAV8-shRrbp1) via tail vein injection (1.8×10^{11} genome copies per mouse) with BD Ultra-Fine Insulin Syringes. Experiments were commenced 21 days after injection.

Inactivation of Mttp with Cre adenovirus in the liver

Liver-specific *Mttp*-knockout mice were generated from *Mttp*-floxed mice (Chang et al., 1999) by injecting male animals (9–12 weeks old) with either control vector (pENN.AAV.TBG.PI.ffLuciferase.RBG, Addgene #105538-AAV8) or AAV.TBG.PI.Cre.rBG (Addgene, #107787-AAV8) via tail vein injection (1.8×10^{10} genome copies per mouse) with BD Ultra-Fine Insulin Syringes. Experiments were commenced 21 days after injection.

MUP bioinformatic analysis

Multiple alignments of amino acid sequences were constructed using MUSCLE (Edgar, 2004). Phylogenetic trees were built using FASTTREE with gamma-distributed site rates and WAG evolutionary model (Price et al., 2010). Protein structure modeling and superposition were performed within the PyMOL computational framework (Janson et al., 2017).

For Figure 4F, the two structures were superimposed with PyMOL, and the potential PA-interacting residues in the MUP cavity were identified under the following criteria: i) being located within 5Å from the palmitic acid in the PTGDS cavity and ii) being structurally aligned with the PTGDS cavity residues as shown in E. The black-labeled residues are the PA-interacting residues of the PTGDS cavity that are identical in the MUP. Both PTGDS and MUP structures are rainbow colored from N to C termini.

Data reporting

No statistical methods were used to predetermine sample size. The experiments were randomized, and the investigators were not blinded to allocation during experiments and outcome assessment. The adhesion sites count has been carried out in parallel by two operators.

QUANTIFICATION AND STATISTICAL ANALYSIS

Unpaired t test was used for comparisons involving two groups, two-way ANOVA was used for multiple pairwise comparisons. For datasets from two groups that did not fulfill the D'Agostino and Pearson omnibus normality test ($\alpha = 0.05$), differences were assessed using a nonparametric two-tailed Mann-Whitney test with 95% confidence.

P-values were calculated using Prism (v. 9, GraphPad Software) as specified in the figure legends. *P*-values of less than 0.05 were considered statistically significant; * $p < 0.05$, ** $p < 0.01$, *** $p < 0.001$, **** $p < 0.0001$. Sample sizes for each experiment is displayed on the figures. Histograms were compiled to include mean ± SEM (standard error of the mean), unless otherwise indicated. For estimation statistics based on confidence intervals (Bernard, 2019; Ho et al., 2019), we directly introduced the raw data in https://www.estimationstats.com/ and downloaded the results and graphs. In these graphs, the mean difference between the groups is depicted as the dot within the vertical error bar that represents the 95% confidence interval.